Title: Optogenetic frequency scrambling of hippocampal theta oscillations dissociates working memory retrieval from hippocampal spatiotemporal codes

Authors: Guillaume Etter[1,*], Suzanne van der Veldt[1], Jisoo Choi[1], Sylvain Williams[1,*]

[1]McGill University & Douglas Mental Health University Institute, Montreal, Canada

* corresponding authors: sylvain.williams@mcgill.ca, 6875 Boulevard LaSalle, Verdun, QC H4H 1R3, Phone: 514 761-6131, Fax: 514 888-4067; etterguillaume@gmail.com

Abstract:

The precise temporal coordination of activity in the brain is thought to be fundamental for memory encoding and retrieval. Pacemaker GABAergic neurons in the medial septum (MS) provide the largest source of innervation to the hippocampus and play a major role in controlling hippocampal theta (~8 Hz) oscillations. While pharmacological inhibition of the MS is known to disrupt memory, the exact role of MS inhibitory neurons and theta frequency rhythms in hippocampal representations and memory is not fully understood. Here, we dissociate the role of theta rhythms in spatiotemporal coding and memory using an all-optical interrogation and recording approach in freely behaving mice. We developed complementary optogenetic stimulation paradigms of MS GABAergic neurons to either pace or abolish theta altogether while recording large hippocampal cell assemblies using calcium imaging conjointly. We first show that optogenetic frequency scrambling of MS GABAergic neuron activity abolished theta rhythms and modulated the activity of a subpopulation of CA1 neurons. Such stimulation led to decreased memory retrieval, but not encoding in both a delayed non-match to sample task, a novel place object recognition task, as well as spontaneous cue-guided linear alternation. Strikingly, scrambled stimulations were not associated with disrupted encoding of place, time, distance, or multiplexed information. Our study suggests that theta rhythms play a specific and essential role in supporting working memory retrieval and maintenance while not being necessary for hippocampal spatiotemporal codes.

Introduction

The precise temporal coordination of neuronal activity is thought to be fundamental for memory encoding and retrieval. In particular, the medial septum (MS) has been proposed to act as the main zeitgeber to downstream structures[1]. It is a neurochemically heterogeneous structure composed of GABAergic[2], mainly parvalbumin (PV)-positive neurons[3], along with cholinergic[4] and a smaller population of glutamatergic neurons[5,6]. MS PV cells project directly onto GABAergic interneurons in the hippocampus giving rise to feedforward inhibitory control of hippocampal pyramidal cells[3]. Additionally, PV interneurons within the hippocampus are essential in pacing theta (~8 Hz) rhythms[7], and optogenetic stimulation of MS-PV neurons directly[8,9] or of their terminals[10] in the hippocampus are associated with frequency-specific pacing of hippocampal oscillations whereas inhibition of the medial septum (MS) *in vivo* has been associated with reduced theta oscillations power[11,12].

While complete MS optogenetic inhibition has been associated with spatial memory impairments[13], these effects could potentially be attributed to disruption of cholinergic functions[14,15], which are known to be critical for memory function. The exact role of non-cholinergic MS PV cells in memory encoding and retrieval remains an active area of research and has only been described recently[16,17]. Since the MS provides the largest subcortical inputs to the hippocampus and is essential in generating and maintaining theta rhythms, disruption of MS activity is likely to impact downstream hippocampal physiology and working memory[18]. Importantly, the hippocampus plays an essential role in encoding and retrieval of episodic[19,20] and working[21] memory. Although the exact physiological mechanisms of hippocampus-dependent memory are currently unknown, it has been proposed that hippocampal place cells[22] that encode specific locations of a given context could support episodic memory[23]. In the hippocampal subfield CA1, spatial tuning relies at least in part on contextual sensory inputs[24]. Other variables such as time and distance can also be encoded during visually guided

57 locomotion[25,26] but also in the absence of sensory cues[27], likely using internal information
58 including self-motion[28] (see Mehta[29] and McNaughton[30] for review). Representations of time
59 and space can be represented conjunctively in hippocampal neurons, and such multiplexed
60 spatiotemporal codes could be a candidate substrate for working memory[31–33]. In addition to
61 clamping distal visual cues using a treadmill[34–36] or using virtual reality paradigms[25,26,37],
62 spatiotemporal codes have also been extracted analytically using generalized linear models
63 that implement space, time, and distance[36] although such approaches have not been employed
64 extensively on recordings of neuronal activity during free exploration.

65 Several studies suggest that hippocampal theta rhythms could underlie temporal codes
66 since theta rhythms tightly orchestrate hippocampal activity[38,39]. While time cells have also
67 been reported in both CA1 and CA3 of rodents performing tasks that do not require working
68 memory[40], pharmacological inhibition of the MS results in specific disruption of time but not
69 place cells and is associated with decreased working memory[35]. An important drawback of
70 pharmacological approaches is that they do not distinguish the relative contribution of
71 GABAergic versus cholinergic cells to memory function[41], and inhibition of MS cholinergic
72 activity was found to alter hippocampal spatial representations[42] and decrease working
73 memory performance[43,44]. Surprisingly, pharmacological inhibition of the MS was associated
74 with reduced theta oscillation power but not place fields[45], and this resilience of place cell
75 activity during diminished theta was not due to experience-related plasticity mechanisms[46].
76 Previous attempts at inhibiting MS GABAergic interneurons specifically using optogenetics
77 were associated with only a partial reduction, but not complete disruption of theta signals[47]. In
78 turn, optogenetic pacing of theta oscillation has only been associated with minor changes in
79 place cell characteristics, including a slight shift in firing frequency[9] and phase[48].
80 Additionally, while it is hypothesized that hippocampal temporal codes could be directly

controlled by MS inputs, causal evidence is still lacking. To this day, the exact role of MS-PV neurons in orchestrating hippocampal spatiotemporal codes and memory remains unknown.

Here we controlled MS PV activity using optogenetics to pace or abolish theta oscillations using a red-shifted excitatory opsin. We propose a novel approach to abolish hippocampal theta rhythms based on optogenetic frequency scrambling stimulations of MS neurons. Alternatively, pacing theta rhythms at their natural frequency in the same animals provides within-subject controls. We combined optogenetic control with calcium imaging of CA1 pyramidal cells in mice running on a linear track with sequential tones. In these conditions, we were able to separate place, time, and distance cells using an information theoretic approach. When performing optogenetic frequency scrambling of theta signals, theta disruption was associated with direct activity modulation in only a small subset of CA1 pyramidal cells. While in these conditions, both place and time modulated cells were preserved, we next found that ablation of theta oscillation was associated with impaired working memory retrieval, but not encoding suggesting that MS PV cells play a key role in generating hippocampal theta oscillations that are necessary for memory retrieval, but are not involved in temporal sequential activity of time modulated cells.

Results

CA1 pyramidal cells encode spatiotemporal information

To examine the spatiotemporal codes in large populations of CA1 principal cells, we injected a viral vector expressing $GCaMP6_{fast}$ under a CamKII promoter in the CA1 region of the hippocampus, implanted a GRIN lens above the injection site, and performed calcium

103 imaging recordings of pyramidal neurons using open-source miniscopes[49,50] (fig. 1a,b; see
104 supplemental fig. 1 for detailed histology). We extracted spatial footprints of neurons (fig. 1c)
105 and their corresponding calcium transients (fig. 1d) using CNMFe[51]. To tease apart the spatial
106 and temporal tuning properties of principal cells, we developed a new task combining a linear
107 track with three tone cues triggered by motion sensors at both ends of the track. A new tone
108 was instantly triggered at the end of each run, informing the mice on its progression toward
109 reward delivery. Every fourth run was cued with a high-pitched, continuous tone that was
110 associated with the delivery of a reward at the end of the linear track (fig. 1e). The absolute
111 location of each mouse, along with the time elapsed and distance traveled since the departure
112 from the reward site were monitored (fig. 1f). Using these variables and binarized neuronal
113 activity, we computed probabilistic tuning curves (fig. 1g) and derived mutual information
114 (MI) between neuronal activity and location, time, as well as the distance for each recorded
115 cell. In contrast to correlation-based analyses, MI does not assume linear, monotonic
116 relationships between neuronal activity and behavioral variables but rather expresses the
117 amount of uncertainty of one variable that can be explained by the other. The significance of
118 MI values was tested using shuffled surrogates that underwent circular permutations (n =
119 1000) to preserve temporal dynamics of calcium transients. Neurons that encoded exclusively
120 one variable with a MI greater than shuffled surrogates 99.5 of the time ($p < 0.005$) were
121 labeled as either place-modulated (spatial), time-modulated (temporal), or distance-modulated
122 (see Methods). For the following analyses, we focused on candidate cells that only encoded
123 one significant variable (fig. 1h). Importantly, time-modulated cells were not systematically
124 active at particular locations, and place-modulated cells were not systematically active at a
125 given time (fig. 1i,j). While the majority of cells encoding a single variable were place-
126 modulated, a large portion of neurons were conjunctive neurons that encoded more than one

127 variable (17.98 ± 1.77 %). In contrast, cells encoding place exclusively represented 9.02 ±
128 1.61 % of the total recorded population, while 1.79 ± 0.68 % selectively encoded distance and
129 1.27 ± 0.09 % selectively encoded time (fig. 1k).

130 Although our information theoretic approach can disentangle overlapping variables by
131 isolating cells that only significantly encode one variable, we further tested the relevance of
132 each cell type in encoding spatiotemporal variables using a naive Bayesian classifier to
133 decode location (fig. 1l-n), time elapsed (fig. 1o-q), and distance traveled (fig. 1r-t) on the
134 linear track[52]. We estimated the current state of each mouse by computing the maximum *a*
135 *posteriori* (MAP) value given neuronal activity and bootstrapped tuning curves computed
136 using either actual or circularly shuffled binarized activity (fig. 1l,o,r; see Methods for
137 detailed protocol). The quality of predictions was assessed using confusion matrices (fig.
138 1m,p,s) and by computing the euclidean distance between predicted state and actual state (fig.
139 1n,q,t). Importantly, we could only decode location using either all cells (paired *t*-test, t_4 = -
140 7.043, p = 0.0021) or place cells only (paired *t*-test, t_4 = -3.780, p = 0.0194). When using any
141 cell but place cells, we could not significantly decode location as decoding error was not
142 significantly different between actual and shuffled datasets (paired *t*-test, t_4 = -1.219, p =
143 0.2896; fig. 1n). While the number of time cells was too low to be used exclusively in our
144 decoder for each mouse, we could only decode time successfully using all cell types (paired *t*-
145 test, t_4 = -4.908, p = 0.0079) or non-place cells (paired *t*-test, t_4 = -3.540, p = 0.2402).
146 Conversely, we were not able to decode time using place cells only (paired *t*-test, t_4 = -1.682,
147 p = 0.1677; fig. 1q), supporting that place cells identified using our method did not carry any
148 substantial temporal codes. Finally, we could decode instantaneous distance traveled only
149 using all cell types (paired *t*-test, t_4 = -7.765, p = 0.0014), but not using only place cells

150 (paired *t*-test, $t_4 = -1.416$, $p = 0.2295$) or non-place cells (paired *t*-test, $t_4 = -2.638$, $p = 0.0576$;
151 fig. 1t).

152

153 **Selective MS optogenetic control of theta oscillations**

154 To examine the relative contribution of MS-generated theta signals to hippocampal
155 spatiotemporal codes, we transfected the red-shifted excitatory opsin ChrimsonR in the MS
156 (fig. 2a). In contrast to inhibitory opsins, ChrimsonR allowed us to either scramble or pace
157 theta signals within subjects. Additionally, ChrimsonR is more effective than the more widely
158 used Channelrhodopsin-2 and provides the capability to combine optogenetics with calcium
159 imaging[53]. 14.91 ± 3.57 % of PV cells expressed ChrimsonR which we found sufficient to
160 exert pervasive control over hippocampal oscillations ($n = 4$ mice; fig. 2b,c). In contrast, we
161 found virtually no expression of ChrimsonR in ChAT cells (1.05 ± 1.052 % of ChAT cells
162 also expressed ChrimsonR; fig. 2d,e).

163 We then implanted mice with fiber optics over the MS and performed 638 nm laser
164 stimulation while recording local field potentials (LFP) in CA1 (fig. 2f). We found that MS
165 scrambled and 8 Hz optogenetic stimulation could disrupt or pace theta oscillations,
166 respectively (fig. 2g). While baseline natural theta displays some frequency variability in the
167 4-12 Hz frequency band, 8 Hz stimulations led to consistent and stable hippocampal
168 oscillations at that frequency, whereas scrambled stimulations consistently abolished theta
169 rhythms (fig. 2h). We found a significant interaction between our stimulation patterns and
170 LFP frequency band ($F_{10} = 6.467$, $p < 0.0001$). In particular, scrambled frequency stimulation
171 significantly decreased theta power (0.341 ± 0.06 portion of baseline theta band power; $p =$
172 0.0394, pairwise t-test), while 8 Hz stimulations significantly increased theta power (3.302 ±

173 0.76 portion of baseline theta band power, p = 0.0004, pairwise t-test; fig. 2i) leaving other
174 frequency bands unaltered.

175 Hippocampal sharp-wave ripples (SWRs) play an essential role in memory
176 consolidation[54–56] and stimulation of MS cholinergic neurons has been associated with reduced
177 ripple activity[57] and impaired working memory[44]. While we found virtually no expression of
178 ChrimsonR in MS cholinergic neurons, it was essential to measure the impact of our MS
179 optogenetic stimulation on ripple physiology. To this end, we recorded CA1-LFP and
180 performed 5s ON-OFF scrambled optogenetic stimulation in freely behaving mice exploring
181 an open-field (fig. 2j). We measured attributes of ripple events before and during scrambled
182 stimulation, and found no changes in power (t-test, t_6 = 0.076, p = 0.941; fig. 2k, left panel),
183 frequency of occurrence (t-test, t_6 = -1.688, p = 0.142; fig. 2l, left panel), or width (t-test, t_6 =
184 0.124, p = 0.905; fig. 2m, left panel). Similarly, applying 8 Hz optogenetic stimulation had no
185 discernable effects on ripple power (t-test, t_6 = 0.378, p = 0.718; fig. 2k, right panel),
186 frequency (t-test, t_6 = -1.643, p = 0.151; fig. 2l, right panel), and width (t-test, t_6 = -0.138, p =
187 0.894; fig. 2m, right panel). Together with our histological results and previous reports that
188 optogenetic stimulation of MS cholinergic neurons reduces the occurrence of SWRs[57], our
189 findings support the notion that these optogenetic stimulations are not affecting cholinergic
190 inputs to the hippocampus.

191

192 **Combining MS optogenetic stimulation and hippocampal calcium imaging**

193 To study the effects of theta manipulations on hippocampal spatial and temporal codes, we
194 combined MS optogenetic stimulation and calcium imaging in CA1. This experimental
195 paradigm raises two potentially important issues: GRIN lens implants involve tissue damage

196 that could alter the physiological state of theta oscillations, and the wavelength spectrum of
197 the excitation LED used to excite GCaMP6f could potentially overlap with that of the opsin
198 located on the terminal fibers of GABAergic MS fibers in the hippocampus.

199 To verify whether GRIN lens implants altered the physiology of theta, we first
200 implanted mice with a GRIN lens in the right hippocampus, with two electrodes in both left
201 and right hippocampi and found comparable theta signals in both hippocampi (fig. 3a). To
202 gain more statistical insights, we compared theta oscillations mice with electrodes only in the
203 right hippocampus, to mice with both a GRIN lens and an attached LFP electrode during open
204 field exploration, and found no significant differences between both groups (fig. 3b). We did
205 not find any significant difference between relative theta power to total LFP power of mice
206 implanted with a GRIN lens and LFP electrode (0.14 ± 0.007) versus an electrode only (0.154
207 ± 0.008; t-test, $t_{54} = 1.060$, $p = 0.29$).

208 Although previous reports have reported that combining optogenetic stimulation of
209 ChrimsonR at the level of cell bodies with calcium imaging of GCaMP6f at the level of
210 terminals is possible with minimal crosstalk[53], we next controlled for any potential opsin
211 activation of MS terminals in the hippocampus by recording CA1-LFP while emitting
212 excitation light with our miniscope through a GRIN lens in mice injected with ChrimsonR in
213 the MS. After calibrating miniscope light output power (fig. 3c), we found no effect of
214 miniscopes blue excitation light on endogenous theta power when using excitation light
215 power below 0.5 mW/mm^2 (1ANOVA, $F_{(4,295)} = 0.7729$, $p = 0.5435$; fig. 3d). Since it has been
216 reported that miniscope excitation light can induce slight depolarization of terminals
217 transfected with ChrimsonR[53], thus hindering further optogenetic-induced depolarization, we
218 next stimulated our control mice while imaging with a ~0.3 mW/mm^2 miniscope LED power

219 and were able to significantly disrupt or pace theta using scrambled or 8 Hz stimulation
220 respectively (Friedman test $\chi^2 = 6$, $p = 0.0278$; fig. 3e).

221

222 **Disruption of theta rhythms modulates a small portion of CA1 cells**

223 We then performed phasic (5s ON, 5s OFF) optogenetic stimulations of MS while recording
224 CA1 pyramidal cells and as mice freely explored an open-field (fig. 4a). We found that a
225 portion of recorded cells were consistently excited in these conditions, while others were
226 inhibited (fig. 4b; see Methods). For one representative mouse, we found that the activity of
227 pyramidal cells during stimulation was overall lower compared to baseline, for both
228 scrambled stimulation during running (Pearson correlation, $R^2 = 0.567.$, $p < 0.0001$) and rest
229 ($R^2 = 0.521$, $p < 0.0001$) periods, as well as for 8 Hz stimulation ($R^2 = 0.6.$, $p < 0.0001$ for rest
230 periods; $R^2 = 0.632.$, $p < 0.0001$ for running periods; fig. 4c). Overall, ~6.42 ± 0.52 % of total
231 cells were significantly modulated by scrambled optogenetic stimulation (fig. 4d). Among
232 those modulated cells, 50.56 ± 6.38 % were inhibited while 49.43 ± 6.38 % were excited
233 during scrambled stimulations (n = 1849 cells, N = 5 mice; fig. 4e).

234

235 **MS optogenetic stimulation alters behavior but not spatiotemporal codes**

236 To assess the effects of theta disruption on temporal and spatial codes, we monitored CA1
237 pyramidal neuron activity on the 3-tone linear track (fig. 5a). Here we leverage one of the
238 main advantages of calcium imaging, which is the ability to register recorded cells over
239 several days, while performing scrambled or 8 Hz stimulations on selected days (fig. 5b; fig.
240 5c, bottom panel). We focused our analysis on pairs of days with the same amount of time

241 (48h) between testing (fig. 5c, top panel). For each condition, we assessed the portion of total
242 cells significantly encoding one or several variables, and found no effect of either 8 Hz or
243 scrambled stimulation on spatial and temporal encoding (RM-ANOVA; $F_2 = 0.807$, $p = 0.453$
244 for the main effect of stimulations; $F_6 = 1.283$, $p = 0.285$ for the interaction between
245 stimulation and encoded variable, n = 5 mice; fig. 5d).

246 While the portion of cells did not change under stimulation conditions, we assessed
247 the effect of MS stimulation on place-, time-, and distance-modulated cells' tuning curves
248 stability. To this end, we tracked neurons across days (see fig. 5c and Methods) and computed
249 stability of place and time fields as the pairwise correlation between fields across 48h.
250 Because CA1 is known to display prominent remapping over days[58], we also used a pair of
251 days with no stimulation to compute a baseline stability score to be used as a reference (fig.
252 5e-g). We found no change in stability during MS stimulation for place-modulated cells
253 (1ANOVA, $F_2 = 1.907$, $p = 0.1511$; fig. 5h), time-modulated cells (1ANOVA, $F_2 = 2.201$, $p =$
254 0.113; fig. 5i), and distance-modulated cells (1ANOVA, $F_2 = 0.6962$, $p = 0.5024$; fig. 5j).

255 Since a large portion of CA1 neurons encode multiple variables conjunctively, we next
256 assessed the quality of spatiotemporal codes using random bootstrap samples (n = 100 cells
257 per sample, n = 50 bootstrap samples) of all recorded cells. Namely, we applied a naive
258 Bayesian classifier to decode location (fig. 6a,b), time (fig. 6c,d), and distance traveled (fig.
259 6e,f). For a representative mouse, decoded errors were systematically lower than shuffled
260 surrogates, including during 8 Hz or scrambled stimulation for location (2ANOVA, $F_{1,294} =$
261 543.9, $p < 0.0001$; fig. 6a), time (2ANOVA, $F_{1,294} = 393.7$, $p < 0.0001$; fig. 6c), and distance
262 (2ANOVA, $F_{1,294} = 1021$, $p < 0.0001$; fig. 6e) indicating that spatiotemporal codes were
263 preserved during stimulation. To gain statistical insights, we z-scored decoding error by using

both the actual and shuffled results (see Methods) for a given day, for every mouse (N = 5 mice; fig. 6b,d,f). MS optogenetic control did not significantly alter encoding of location (1ANOVA, $F_{2,11} = 3.8$, $p = 0.0544$; fig. 6b), time (1ANOVA, $F_{2,11} = 3.001$, $p = 0.0912$; fig. 6d), or distance (1ANOVA, $F_{2,11} = 3.398$, $p = 0.0709$; fig. 6f).

In the behavioral paradigm used to analyze temporal modulation of neuronal activity, mice are water-scheduled and expected to collect rewards as quickly as possible. Based on this assumption, we quantified the number of returns to an empty reward site as errors, and computed the percentage of correct runs to total runs as a proxy for performance (fig. 6g). In these conditions we found a significant effect of optogenetic stimulation on performance across days (Friedman test $\chi^2 = 6.000$, $p = 0.0278$) and in particular a significant difference in performance between during baseline (78.70 ± 2.45 %) and scrambled stimulation (44.44 ± 5.56 %; multiple comparison, $p = 0.0429$; N = 3 mice; fig. 6h). Only mice with a minimum of 12 runs were included in this analysis. Because of the limitations of this task (low cognitive load and low number of mice tested), we next set out to assess the effect of MS optogenetic stimulation in standardized behavioral tasks. Importantly, it was previously reported that pacing theta oscillations could decrease locomotor speed and its variability[10]. To thoroughly assess the specificity of MS optogenetic stimulation on memory, we performed additional experiments to rule out the direct effects of the optogenetic stimulations on locomotor velocity.

Locomotor speed dictates theta frequency, but optogenetic control does not control speed

286 A subset of mice injected with ChrimsonR in the MS and implanted with fiber optics in the
287 MS and LFP electrodes in CA1 were allowed to explore an open-field freely while being
288 subjected to 5s ON, 5s OFF optogenetic stimulations (fig. 7a). Consistently, 8 Hz stimulation
289 led to consistent pacing of hippocampal oscillations to that frequency (fig. 7b). Those
290 stimulations were not associated with any apparent change in locomotor behavior (fig. 7c),
291 including mean speed (t-test, $t_{116} = 0.4140$, $p = 0.6796$; fig. 7d) and speed coefficient of
292 variation (CV; t-test, $t_{116} = 0.8296$, $p = 0.4095$, n = 59 stimulation epochs; fig. 7e). Similarly,
293 scrambled stimulation consistently led to abolished theta oscillations (fig. 7f) but no apparent
294 changes in locomotor behavior (fig. 7g), including mean speed (t-test, $t_{118} = 0.2268$, $p =$
295 0.8210; fig. 7h) and speed CV (t-test, $t_{118} = 1.838$, $p = 0.686$, n = 60 stimulation epochs; fig.
296 7i).

297 While natural theta frequency and locomotor speed are correlated[59], the exact direction
298 of causation between these variables remains poorly understood. To answer this question, we
299 performed optogenetic stimulation using a 5s ON, 5s OFF paradigm and a random frequency
300 was selected for each stimulation epoch (fig. 7j). These stimulation frequencies covered the
301 entirety of the theta band spectrum (fig. 7k). As expected, we found that natural theta
302 oscillations frequencies are directly correlated to running speed for one example mouse ($R^2 =$
303 0.1114, $p < 0.0001$; fig. 7l). Importantly, when theta oscillation frequency results from MS
304 optogenetic control, the correlation drops below chance level ($R^2 = 0.0006779$, $p = 0.6244$;
305 fig. 7m) suggesting that locomotion dictates theta frequency, but not the opposite. We
306 systematically replicated these results across mice and observed a drop in the correlation
307 between theta frequency and locomotor speed under optogenetic stimulation control (paired t-
308 test, $t_3 = 3.922$, $p = 0.0295$; fig. 7n). Altogether, these results support that our optogenetic

309 stimulation does not alter locomotor behavior, which is highly relevant for the next behavioral
310 assays.

311

312 **Disruption of theta signals impairs working memory maintenance and retrieval, but not**
313 **encoding**

314 To test the role of theta signals in spatial memory, we prepared a dedicated group of mice
315 injected with ChrimsonR and implanted with a fiber optic in the MS (fig. 8a, left panel). Mice
316 were subjected to a novel place object recognition (NPOR) task (fig. 8a, right panel). To
317 assess the role of theta oscillations in memory retrieval, we performed optogenetic
318 stimulations specifically during testing and computed recognition index (RI; see Methods). In
319 these conditions, memory performance was significantly reduced for both scrambled (0.472 ±
320 0.048 RI, n = 6 mice) and 8 Hz stimulations (0.435 ± 0.057 RI, n = 6 mice) groups, compared
321 to YFP controls that displayed a significant increase in object exploration during testing (0.61
322 ± 0.018 RI, n = 12 mice; 2ANOVA, $p = 0.0097$; fig. 8b).

323 To further examine the effect of optogenetic control of the MS on specific phases of
324 working memory function (encoding, maintenance, and retrieval), mice were transfected with
325 ChrimsonR and implanted with fiber optics in the MS and trained in a delayed non-match to
326 sample (DNMTS) task. In the sample phase, mice were forced to run to a randomly
327 designated arm to collect a reward. After a delay (10 s), they could either run in the opposite
328 arm (correct choice) to receive another reward, or run in the same, unrewarded arm (incorrect
329 arm; fig. 8c). The advantage of this task is to allow for repetitive testing, specific isolation of
330 task phases (training, delay, testing) and within-subject controls. Mice were trained in this
331 task with no stimulation until criterion performance of 0.8 (portion of correct trials) was

332 reached for at least two days. Both ChrimsonR and YFP control mice displayed significant
333 improvement over time (RMANOVA, $F_8 = 8.737$, $p < 0.0001$ for the main effect of training
334 days). Importantly, we found no learning rate differences between the two groups (pairwise
335 Tukey; $p = 0.42$; fig. 8d). Once mice had learned the rule associated with the DNMTS task,
336 we assessed performance while delivering either scrambled (0.792 ± 0.045) or 8 Hz (0.850 ±
337 0.036) optogenetic stimulation in the encoding phase (forced choice) only, and did not
338 observe any difference in performance compared to baseline (0.825 ± 0.030, RM-ANOVA,
339 $F_{11} = 2.197$, $p = 0.547$, n = 12; fig. 8e). When stimulated only during the delay period, only
340 scrambled stimulations significantly decreased memory performance (0.733 ± 0.057)
341 compared to baseline (0.825 ± 0.030, RM-ANOVA, $F_{11} = 3.483$, $p = 0.0495$; fig. 8f). In
342 contrast, when stimulated during retrieval, mice stimulated with 8 Hz displayed significantly
343 reduced memory performance (0.675 ± 0.049) compared to baseline (0.825 ± 0.030, RM-
344 ANOVA, $F_{11} = 3.265$, $p = 0.050$; fig. 8g). In contrast, YFP control mice were not affected by
345 stimulations during encoding (RM-ANOVA, $F_2 = 0.1314$, $p = 0.8781$), the delay period (RM-
346 ANOVA, $F_2 = 0.2020$, $p = 0.8197$), or retrieval (RM-ANOVA, $F_2 = 0.0454$, $p = 0.9557$) of
347 working memory.

348

349 **Discussion**

350 Within the septohippocampal system, the exact causal relationships between (1) MS activity,
351 (2) hippocampal oscillations, (3) hippocampal neuron activity, and (4) behavior including
352 memory remain an active area of research. In particular, whether and how the MS supports
353 encoding of place and time in the hippocampus, as well as its specific contribution to memory
354 function remain unclear. Here, we leveraged more recent techniques that allowed us to record

355 >1000 neurons while performing optogenetic stimulation of MS neurons with a sub-second
356 resolution to control theta rhythms and assess its role in hippocampal physiology and
357 memory. Importantly, using an excitatory opsin and either scrambled or 8 Hz stimulations, we
358 were able to consistently and robustly abolish or pace hippocampal theta respectively.
359 Compared to MS inhibition using either an inhibitory opsin or pharmacological compounds
360 (e.g. muscimol), our approach enables a within-subject comparison of two opposed states
361 (paced vs abolished theta) while maintaining activity levels in MS-PV cells. We combined a
362 novel tone-cued linear track task that, together with information theoretic approaches, allowed
363 us to disentangle spatial and temporal hippocampal codes. This method alleviates the need for
364 arbitrary thresholds, enabling a standardized approach to calcium imaging analysis as
365 described previously[52]. While a large portion of CA1 pyramidal neurons expressed a mixture
366 of spatiotemporal codes, we focused our analyses on neurons tuned specifically to place, time,
367 or distance traveled.

368 While spatial coding has been extensively investigated in CA1, temporal and distance
369 codes have recently gained more interest. Temporal[27,34–36] and distance[36] codes have been
370 extracted by clamping visuospatial cues or extracted analytically using generalized linear
371 models in virtual reality paradigms[25,26,37]. Here we propose a novel approach to disentangle
372 spatial, temporal, and distance codes using an information theoretic approach which, together
373 with our novel cued-alternation task, enables the analysis of real world spatiotemporal and
374 multiplexed codes in freely moving animals. Strikingly, we confirm previous reports that a
375 large amount of CA1 pyramidal neurons encode multiplexed information of location,
376 distance, and time[25,26,37] in addition to self-motion signals such as acceleration, speed, and
377 orientation[60].

In this context, frequency scrambling and 8 Hz optogenetic stimulations drastically abolished or paced theta rhythms, respectively, and led to an overall decreased activity in a subpopulation of CA1 pyramidal cells. Our optogenetic scrambling stimulations of the MS were not associated with significant changes in place cell activity, similar to previous reports using either pharmacological inhibition[35,45,46], or optogenetic[9,48] pacing of MS or septal inputs to the hippocampus. As MS neurons are known to be the primary driver of hippocampal oscillations, we expected that MS stimulation would be associated with disrupted time or distance cell activity in conditions of reduced theta rhythms, but did not observe any change for both abolished and paced theta conditions. Additionally, pacing of hippocampal oscillations to 8 Hz did not lead to changes in the quality of spatial codes as reported previously[9], and did not alter temporal codes as observed in our behavioral paradigm.

While it was reported that time (but not place) cells could depend directly on medial entorhinal cortex (MEC) inputs[61], other studies show that MEC lesions do not lead to any alterations in hippocampal time cell physiology[62]. Notably, a more recent investigation found that optogenetic pacing of the MS did not disrupt the spatial codes of grid cells in the entorhinal cortex[63], further suggesting that MS activity is not directly involved in spatial codes within the hippocampal formation. Together with our results, this indicates that temporal codes could either be the result of MS-dependent computations within the entorhinal cortex[63] (1), or be generated intrinsically within the hippocampus itself (2).

While early studies found that the MS played an essential role in maintaining time cells and supporting working memory[35], recent experimental evidence shows that the exact contribution of time cells to working memory performance could be less than previously thought[62]. Since MS-PV neurons likely maintain significant activity levels during frequency

401 scrambling optogenetic stimulation (in contrast to inhibition approaches), our results strongly
402 support the role of precisely timed septal activity in supporting working memory, as
403 hypothesized previously[18]. Although we observed reduced memory performance when using
404 optogenetic stimulation during retrieval for the novel object place recognition and the delayed
405 non-match to sample tasks, stimulation during the encoding phase was not associated with
406 reduced memory. We provide experimental evidence that manipulation of MS does not alter
407 locomotor speed and that conversely, locomotor speed does dictate theta frequency. Even
408 though place and time codes were preserved during our MS stimulations, a portion (~6%) of
409 cells were directly modulated, and could account for memory impairments observed in our
410 behavioral assays. PV interneurons in the hippocampus have previously been reported to be
411 part of a microcircuit essential in regulating memory consolidation[64,65], and our optogenetic
412 manipulations could be associated with silencing of these cells to some extent. Moreover,
413 although we did not observe changes in frequency bands other than theta, we cannot exclude
414 that CA1 pyramidal neuron spike timing could be drastically altered when scrambling theta
415 oscillations, while 8 Hz stimulation were shown to not result in increased hippocampal
416 activity[17], which could explain the differential effects of those stimulation patterns on working
417 memory performance. The memory impairments we observed were likely non-cholinergic:
418 firstly, in our immunohistological experiments we found virtually no expression of
419 ChrimsonR in ChAT neurons of the MS. Secondly, our optogenetic stimulations were not
420 associated with changes in hippocampal ripples, while previous reports indicate that ChAT
421 neurons stimulation is associated with reduced ripple frequency[44,57]. ChrimsonR transfection
422 of MS VGLUT2 neurons is also unlikely, since activation of these neurons is associated with
423 direct increase in locomotor activity[66], which we did not observe. Although the precise
424 temporal arrangement of CA1 pyramidal spikes could explain, at least partially, the effects of

425 MS stimulation on memory, alternative mechanisms should be taken into consideration.
426 Notably, in addition to the hippocampus and the entorhinal cortex, MS PV neurons project to
427 the retrosplenial cortex[3], and could be responsible for some of the memory impairments
428 observed here.

429 In summary, using calcium imaging, optogenetics, and electrophysiology, we found
430 that theta rhythms can be paced or abolished using stimulation of the MS. Such stimulation
431 impaired memory retrieval and maintenance, but not encoding. These effects were non-
432 cholinergic, and did not disrupt hippocampal ripple activity. Finally, while a small fraction of
433 hippocampal neurons respond directly to optogenetic stimulation of the MS, place, time, and
434 distance cells are not disrupted by reduced theta oscillations. Together these results suggest
435 that while MS input to the hippocampus plays an essential role in memory, multiplexed codes
436 in CA1 pyramidal neurons might not be the direct substrate for such functions.

437

438

439 **References**

440 1. Colgin, L. L. Rhythms of the hippocampal network. *Nat. Rev. Neurosci.* **17**, 239–249
441 (2016).
442 2. Tóth, K., Freund, T. F. & Miles, R. Disinhibition of rat hippocampal pyramidal cells by
443 GABAergic afferents from the septum. *J. Physiol.* **500**, 463–474 (1997).
444 3. Unal, G., Joshi, A., Viney, T. J., Kis, V. & Somogyi, P. Synaptic targets of medial septal
445 projections in the hippocampus and extrahippocampal cortices of the mouse. *J. Neurosci.*
446 **35**, 15812–15826 (2015).
447 4. Simon, A. P., Poindessous-Jazat, F., Dutar, P., Epelbaum, J. & Bassant, M.-H. Firing
448 properties of anatomically identified neurons in the medial septum of anesthetized and
449 unanesthetized restrained rats. *J. Neurosci.* **26**, 9038–9046 (2006).
450 5. Sotty, F. *et al.* Distinct electrophysiological properties of glutamatergic, cholinergic and
451 GABAergic rat septohippocampal neurons: novel implications for hippocampal
452 rhythmicity. *J. Physiol.* **551**, 927–943 (2003).
453 6. Manseau, F., Danik, M. & Williams, S. A functional glutamatergic neurone network in the
454 medial septum and diagonal band area. *J. Physiol.* **566**, 865–884 (2005).
455 7. Amilhon, B. *et al.* Parvalbumin interneurons of hippocampus tune population activity at
456 theta frequency. *Neuron* **86**, 1277–1289 (2015).
457 8. Etter, G. *et al.* Optogenetic gamma stimulation rescues memory impairments in an
458 Alzheimer's disease mouse model. *Nat. Commun.* **10**, 1–11 (2019).
459 9. Zutshi, I. *et al.* Hippocampal neural circuits respond to optogenetic pacing of theta
460 frequencies by generating accelerated oscillation frequencies. *Curr. Biol.* **28**, 1179-1188.e3
461 (2018).
462 10. Bender, F. *et al.* Theta oscillations regulate the speed of locomotion via a

463 hippocampus to lateral septum pathway. *Nat. Commun.* **6**, 8521 (2015).

464 11. Green, J. D. & Arduini, A. A. Hippocampal electrical activity in arousal. *J.*
465 *Neurophysiol.* **17**, 533–557 (1954).

466 12. Mitchell, S. J., Rawlins, J. N., Steward, O. & Olton, D. S. Medial septal area lesions
467 disrupt theta rhythm and cholinergic staining in medial entorhinal cortex and produce
468 impaired radial arm maze behavior in rats. *J. Neurosci.* **2**, 292–302 (1982).

469 13. Gemzik, Z. M., Donahue, M. M. & Griffin, A. L. Optogenetic suppression of the
470 medial septum impairs working memory maintenance. *Learn. Mem.* **28**, 361–370 (2021).

471 14. Knox, D. & Keller, S. M. Cholinergic neuronal lesions in the medial septum and
472 vertical limb of the diagonal bands of Broca induce contextual fear memory generalization
473 and impair acquisition of fear extinction. *Hippocampus* **26**, 718–726 (2016).

474 15. Jeong, D. U. *et al.* Improvements in memory after medial septum stimulation are
475 associated with changes in hippocampal cholinergic activity and neurogenesis. *BioMed*
476 *Res. Int.* **2014**, e568587 (2014).

477 16. Sans-Dublanc, A. *et al.* Septal GABAergic inputs to CA1 govern contextual memory
478 retrieval. *Sci. Adv.* **6**, eaba5003 (2020).

479 17. Quirk, C. R. *et al.* Precisely timed theta oscillations are selectively required during the
480 encoding phase of memory. *Nat. Neurosci.* **24**, 1614–1627 (2021).

481 18. Mehta, M. R. Role of Rhythms in Facilitating Short-Term Memory. *Neuron* **45**, 7–9
482 (2005).

483 19. Scoville, W. B. & Milner, B. Loss of recent memory after bilateral hippocampal
484 lesions. *J Neurol Neurosurg Psychiat* **20**, 11–21 (1957).

485 20. Penfield, W. & Milner, B. Memory deficit produced by bilateral lesions in the
486 hippocampal zone. *AMA Arch. Neurol. Psychiatry* **79**, 475–497 (1958).

21. Jeneson, A. & Squire, L. R. Working memory, long-term memory, and medial temporal lobe function. *Learn. Mem.* **19**, 15–25 (2012).

22. O'Keefe, J. & Dostrovsky, J. The hippocampus as a spatial map. Preliminary evidence from unit activity in the freely-moving rat. *Brain Res.* **34**, 171–175 (1971).

23. Robinson, N. T. M. *et al.* Targeted Activation of Hippocampal Place Cells Drives Memory-Guided Spatial Behavior. *Cell* **183**, 1586-1599.e10 (2020).

24. Muller, R. U. & Kubie, J. L. The effects of changes in the environment on the spatial firing of hippocampal complex-spike cells. *J. Neurosci.* **7**, 1951–1968 (1987).

25. Ravassard, P. *et al.* Multisensory Control of Hippocampal Spatiotemporal Selectivity. *Science* **340**, 1342–1346 (2013).

26. Aghajan, Z. M. *et al.* Impaired spatial selectivity and intact phase precession in two-dimensional virtual reality. *Nat. Neurosci.* **18**, 121–128 (2015).

27. Villette, V., Malvache, A., Tressard, T., Dupuy, N. & Cossart, R. Internally recurring hippocampal sequences as a population template of spatiotemporal information. *Neuron* **88**, 357–366 (2015).

28. Samsonovich, a & McNaughton, B. L. Path integration and cognitive mapping in a continuous attractor neural network model. *J. Neurosci. Off. J. Soc. Neurosci.* **17**, 5900–20 (1997).

29. Mehta, M. R. From synaptic plasticity to spatial maps and sequence learning: Place Field Plasticity. *Hippocampus* **25**, 756–762 (2015).

30. McNaughton, B. L., Battaglia, F. P., Jensen, O., Moser, E. I. & Moser, M.-B. Path integration and the neural basis of the 'cognitive map'. *Nat. Rev. Neurosci.* **7**, 663–78 (2006).

31. Eichenbaum, H. Time cells in the hippocampus: a new dimension for mapping

511 memories. *Nat. Rev. Neurosci.* **15**, 732–744 (2014).
512 32. Eichenbaum, H. On the Integration of Space, Time, and Memory. *Neuron* **95**, 1007–
513 1018 (2017).
514 33. Eichenbaum, H. The role of the hippocampus in navigation is memory. *J.*
515 *Neurophysiol.* **117**, 1785–1796 (2017).
516 34. Pastalkova, E. Internally Generated Cell Assembly Sequences in the Rat Hippocampus
517 Eva Pastalkova. **1322**, (2012).
518 35. Wang, Y., Romani, S., Lustig, B., Leonardo, A. & Pastalkova, E. Theta sequences are
519 essential for internally generated hippocampal firing fields. *Nat. Neurosci.* **18**, 282–288
520 (2015).
521 36. Kraus, B. J., Robinson, R. J., White, J. A., Eichenbaum, H. & Hasselmo, M. E.
522 Hippocampal 'time cells': time versus path integration. *Neuron* **78**, 1090–1101 (2013).
523 37. Moore, J. J., Cushman, J. D., Acharya, L., Popeney, B. & Mehta, M. R. Linking
524 hippocampal multiplexed tuning, Hebbian plasticity and navigation. *Nature* **599**, 442–448
525 (2021).
526 38. O'Keefe, J. & Recce, M. L. Phase relationship between hippocampal place units and
527 the EEG theta rhythm. *Hippocampus* **3**, 317–330 (1993).
528 39. Skaggs, W. E., McNaughton, B. L., Wilson, M. A. & Barnes, C. A. Theta phase
529 precession in hippocampal neuronal populations and the compression of temporal
530 sequences. *Hippocampus* **6**, 149–172 (1996).
531 40. Salz, X. D. M. *et al.* Time cells in hippocampal area ca3. **36**, 7476–7484 (2016).
532 41. Givens, B. S. & Olton, D. S. Cholinergic and GABAergic modulation of medial septal
533 area: Effect on working memory. *Behav. Neurosci.* **104**, 849–855 (1990).
534 42. Ikonen, S., McMahan, R., Gallagher, M., Eichenbaum, H. & Tanila, H. Cholinergic

535 system regulation of spatial representation by the hippocampus. *Hippocampus* **12**, 386–397
536 (2002).
537 43. Givens, B. S., Olton, D. S. & Crawley, J. N. Galanin in the medial septal area impairs
538 working memory. *Brain Res.* **582**, 71–77 (1992).
539 44. Zhang, Y. *et al.* Cholinergic suppression of hippocampal sharp-wave ripples impairs
540 working memory. *Proc. Natl. Acad. Sci.* **118**, (2021).
541 45. Koenig, J., Linder, A. N., Leutgeb, J. K. & Leutgeb, S. The spatial periodicity of grid
542 cells is not sustained during reduced theta oscillations. *Science* **332**, 592–595 (2011).
543 46. Brandon, M. P., Koenig, J., Leutgeb, J. K. & Leutgeb, S. New and distinct
544 hippocampal place codes are generated in a new environment during septal inactivation.
545 *Neuron* **82**, 789–796 (2014).
546 47. Boyce, R., Glasgow, S. D., Williams, S. & Adamantidis, A. Sleep research: Causal
547 evidence for the role of REM sleep theta rhythm in contextual memory consolidation.
548 *Science* **352**, 812–816 (2016).
549 48. Mouchati, P. R., Kloc, M. L., Holmes, G. L., White, S. L. & Barry, J. M. Optogenetic
550 "low-theta" pacing of the septohippocampal circuit is sufficient for spatial goal finding and
551 is influenced by behavioral state and cognitive demand. *Hippocampus* (2020)
552 doi:10.1002/hipo.23248.
553 49. Aharoni, D. & Hoogland, T. M. Circuit investigations with open-source miniaturized
554 microscopes: past, present and future. *Front. Cell. Neurosci.* **13**, (2019).
555 50. Ghosh, K. K. *et al.* Miniaturized integration of a fluorescence microscope. *Nat.*
556 *Methods* **8**, 871–878 (2011).
557 51. Zhou, P. *et al.* Efficient and accurate extraction of in vivo calcium signals from
558 microendoscopic video data. *eLife* **7**, e28728 (2018).

52. Etter, G., Manseau, F. & Williams, S. A probabilistic framework for decoding behavior from in vivo calcium imaging data. *Front. Neural Circuits* **14**, (2020).

53. Stamatakis, A. M. *et al.* Simultaneous optogenetics and cellular resolution calcium imaging during active behavior using a miniaturized microscope. *Front. Neurosci.* **12**, 1–16 (2018).

54. Buzsáki, G. Hippocampal sharp wave-ripple: A cognitive biomarker for episodic memory and planning. *Hippocampus* **25**, 1073–1188 (2015).

55. Roux, L., Hu, B., Eichler, R., Stark, E. & Buzsáki, G. Sharp wave ripples during learning stabilize the hippocampal spatial map. *Nat. Neurosci.* **20**, 845–853 (2017).

56. Fernández-Ruiz, A. *et al.* Long-duration hippocampal sharp wave ripples improve memory. *Science* **364**, 1082–1086 (2019).

57. Vandecasteele, M. *et al.* Optogenetic activation of septal cholinergic neurons suppresses sharp wave ripples and enhances theta oscillations in the hippocampus. *Proc. Natl. Acad. Sci. U. S. A.* **111**, (2014).

58. Ziv, Y. *et al.* Long-term dynamics of CA1 hippocampal place codes. *Nat. Publ. Group* **16**, 264–266 (2013).

59. Sławińska, U. & Kasicki, S. The frequency of rat's hippocampal theta rhythm is related to the speed of locomotion. *Brain Res.* **796**, 327–331 (1998).

60. Veldt, S. van der, Etter, G., Mosser, C.-A., Manseau, F. & Williams, S. Conjunctive spatial and self-motion codes are topographically organized in the GABAergic cells of the lateral septum. *PLOS Biol.* **19**, e3001383 (2021).

61. Robinson, N. T. M. *et al.* Medial entorhinal cortex selectively supports temporal coding by hippocampal neurons. *Neuron* **94**, 677-688.e6 (2017).

62. Sabariego, M. *et al.* Time cells in the hippocampus are neither dependent on medial

583 entorhinal cortex inputs nor necessary for spatial working memory. *Neuron* **102**, 1235-
584 1248.e5 (2019).
585 63. Lepperød, M. E. *et al.* Optogenetic pacing of medial septum parvalbumin-positive
586 cells disrupts temporal but not spatial firing in grid cells. *Sci. Adv.* **7**, eabd5684.
587 64. Xia, F. *et al.* Parvalbumin-positive interneurons mediate neocortical-hippocampal
588 interactions that are necessary for memory consolidation. *eLife* **6**, 1–25 (2017).
589 65. Donato, F., Rompani, S. B. & Caroni, P. Parvalbumin-expressing basket-cell network
590 plasticity induced by experience regulates adult learning. *Nature* **504**, 272–276 (2013).
591 66. Fuhrmann, F. *et al.* Locomotion, theta oscillations, and the speed-correlated firing of
592 hippocampal neurons are controlled by a medial septal glutamatergic circuit. *Neuron* **86**,
593 1253–1264 (2015).
594 67. Paxinos, G. & Watson, C. The rat brain in stereotaxic coordinates. *Acad. Press Inc*
595 439 (1997) doi:10.1016/0166-2236(87)90017-8.
596 68. Mathis, A. *et al.* DeepLabCut: markerless pose estimation of user-defined body parts
597 with deep learning. *Nat. Neurosci.* **21**, 1281–1289 (2018).
598 69. Nath, T. *et al.* Using DeepLabCut for 3D markerless pose estimation across species
599 and behaviors. *Nat. Protoc.* **14**, 2152–2176 (2019).
600 70. Pnevmatikakis, E. A. & Giovannucci, A. NoRMCorre: An online algorithm for
601 piecewise rigid motion correction of calcium imaging data. *J. Neurosci. Methods* **291**, 83–
602 94 (2017).
603 71. Cohen, M. X. *Analyzing neural time series data: theory and practice*. (The MIT Press,
604 2014).
605 72. Sheintuch, L. *et al.* Tracking the same neurons across multiple days in ca2+ imaging
606 data. *Cell Rep.* **21**, 1102–1115 (2017).

73. Wikenheiser, A. M. & Redish, A. D. The balance of forward and backward hippocampal sequences shifts across behavioral states. *Hippocampus* **23**, 22–29 (2013).

610 **Methods**

611 **Animals**

612 All procedures were approved by the McGill University Animal Care Committee and the
613 Canadian Council on Animal Care (protocol 2015-7650). A total of n = 41 male and female
614 (8-16 weeks old) parvalbumin-cre mice (Jackson Laboratory) were used in this study. Mice
615 were housed individually on a 12-hour light/dark cycle at 22°C and 40% humidity with food
616 and water ad libitum. All experiments were carried out during the light portion of the
617 light/dark cycle.

618

619 **Adeno-associated viral vectors**

620 Adeno-associated virus AAV5.CamKII.GCaMP6f.WPRE.SV40 (Addgene # 100834,
621 obtained from University of Pennsylvania Vector Core) was used in all calcium imaging
622 experiments. Adeno-associated virus (AAV) of serotype *dj* (hybrid capsid created from 8
623 different AAV serotypes) AAVdj-hSyn-ChrimsonR-tdTomato were obtained from the Vector
624 Core Facility at Oregon Health and Science University in Portland, Oregon. Although hSyn is
625 a housekeeping gene, we did not observe transfection in cholinergic cells (see Results and fig.
626 2b-e). An eYFP construct without the ChrimsonR sequence was used as a control (termed
627 YFP control in this manuscript).

628

629 **Surgical procedures**

630 Mice were anesthetized with isoflurane (5% induction, 0.5-1 % maintenance) and placed in a
631 stereotaxic frame (David Kopf Instruments). Body temperature was maintained with a heating
632 pad, eyes were hydrated with gel (Optixcare), and Carprofen (10 ml/kg) was administered

633 subcutaneously. The skull was completely cleared of all connective tissue and small
634 craniotomies were performed using a dental drill for subsequent injection or implant.

635

636 *Viral injections*

637 All viral injections were performed using a glass pipette connected to a Nanoject III
638 (Drummond) injector at a flow rate of 1 nL/second. 500 nl of AAVdj-hSyn-ChrimsonR-
639 tdTomato (or eYFP control) was delivered into the medial septum at a rate of 1 nL/s, at the
640 following coordinates based on reference mouse stereotaxic atlas[67] (distance from Bregma in
641 mm): anteroposterior (AP) 0.85, mediolateral (ML) 0, dorsoventral (DV) −4.50 using a 5º
642 angle in the ML plane. After surgery, animals were continuously monitored until recovery.

643

644 *Fiber optic implant*

645 Two weeks post-injection, mice were anesthetized for implantation following the same
646 surgical procedure. 200 μm diameter fiber optics with ceramic ferrule (Thor labs) were
647 implanted at the same coordinates. Implants were cemented in place using C&B-Metabond®
648 (Patterson dental, MN). Black nail polish was applied over the dental cement to block light
649 emission during optogenetic stimulation.

650

651 *Electrode implants*

652 An array of 7 tungsten microelectrodes (~1 MΩ impedance) was lowered in dorsal CA1
653 spanning through *stratum pyramidale* (pyr), *stratum radiatum* (rad) and *stratum lacunosum*
654 *moleculare* (lm). Screws placed in the bone above the frontal cortex and cerebellum served as
655 ground and reference, respectively. Following electrode, ground and reference placement,
656 dental cement was applied to secure the implant permanently to the skull.

657

658 *Implant for calcium imaging*

659 We injected the AAV5.CamKII.GCaMP6f virus (200 nL at 1 nl.s–1) in hippocampal CA1
660 using the following coordinates: anteroposterior (AP) −1.86 mm from bregma, mediolateral
661 (ML) 1.5 mm, dorsoventral (DV) 1.5 mm. 2 weeks following the injection, the mouse was
662 anesthetized with isoflurane and the skull was cleared. A ~2 mm diameter craniotomy was
663 performed in the skull above the injection site. An anchor screw was placed on the posterior
664 plate above the cerebellum. The dura was removed, and the portion of the cortex above the
665 injection site was aspirated using a vacuum pump, until the corpus callosum was visible.
666 These fiber bundles were then gently aspirated without applying pressure on the underlying
667 hippocampus, and a 1.8 mm diameter gradient index (GRIN; Edmund Optics) lens was
668 lowered at the following coordinates: AP −1.86 mm from bregma, ML 1.5 mm, DV 1.2 mm.
669 The GRIN lens was permanently attached to the skull using C&B-Metabond (Patterson
670 Dental), and Kwik-Sil (World Precision Instruments) silicone adhesive was placed on the
671 GRIN to protect it. 4 weeks later, the silicone cap was removed and CA1 was imaged using a
672 miniscope mounted with an aluminum base plate while the mouse was under light anesthesia
673 (~0.5 % isoflurane) to allow the visualization of cell activity. When a satisfying field of view
674 was found (large neuronal assembly, visible landmarks), the base plate was cemented above

675 the GRIN lens, the miniscope was removed, and a plastic cap was placed on the base plate to
676 protect the GRIN lens.

677

678 *Simultaneous calcium imaging and electrophysiological recordings*

679 To control for the effects of GRIN implants on theta physiology as well as cross-talk between
680 miniscope and optogenetic excitation lights, we attached tungsten micro-electrodes to GRIN
681 lenses. To this end, we placed GRIN lenses horizontally under a low-magnification
682 microscope in a dust-free environment. A tungsten microelectrode was gently placed on the
683 top-edge of the GRIN lens using a micromanipulator. We used the known diameter of the
684 GRIN lens as a reference unit to estimate the desired protrusion of the electrode (~50µm,
685 further assessed digitally after taking a microphotograph of the preparation) in accordance
686 with our planned implantation coordinates. Small amounts (~50µL) of superglue were
687 deposited on the top edge of the GRIN lens with the electrode in place, left to dry for ~10min,
688 before applying the next layer of glue. 5 thin layers were used to maintain the electrode
689 attached to the GRIN lens. After implantation of these GRIN-electrode assemblies using the
690 protocol described above, the protruding wires were gently bent and hidden under a protective
691 cap (1-1.5 cm high) retrieved from the pear of a manual suction pipette as a replacement for
692 Kwik-Sil.

694 ***In vivo* behavioral procedures**

695 *Habituation*

696 Mice were habituated by being gently handled for ~5 min over the course of one week, with
697 progressive habituation to the plugging procedure (fiber optic, baseplate, and
698 electrophysiological pre-amplified tethers. Animals were then water-scheduled (2h access per
699 day). Miniscope recordings were performed at 30 Hz for 15 minutes, with only one recording
700 session per day to minimize photobleaching.
701

702 *Miniscope recordings*

703 Miniscopes (V3) were assembled using open-source instructions as described previously
704 (miniscope.org). Imaging data were acquired using a CMOS imaging sensor (Aptina,
705 MT9V032) and multiplexed through a lightweight coaxial cable. Data was acquired using a
706 data acquisition (DAQ) box connected via a USB host controller (Cypress, CYUSB3013).
707 Animal behavior was recorded using a consumer grade webcam (Logitech) mounted above
708 the environment. Calcium and behavioral data were recorded using miniscope.org open
709 source DAQ custom acquisition software. The DAQ simultaneously acquired behavioral and
710 cellular imaging streams at 30 Hz as uncompressed .avi files of 1000 frames, along with
711 timestamps to enable precise temporal alignment of behavioral and calcium imaging data.

712

713 *In vivo electrophysiological recordings*

714 Following 1 week of post-surgical recovery and one week of habituation to the tethering
715 setup, LFP from implanted mice was recorded. All recorded signals from implanted
716 electrodes were amplified by the tether pre-amplifier before being digitized at 22 KHz using a
717 digital recording system (Neuralynx, USA). Recordings of each channel signal were saved in

718 a dedicated file along with video recordings and TTL signals from the Laser Diode for
719 subsequent analysis.

720

721 *Optogenetic stimulation*

722 Laser stimulation was delivered through a fiber optic cord (200 µm diameter) using a laser
723 diode fiber light source (Doric Lenses). Light intensity was calibrated and wavelength-
724 corrected using the Power Meter Bundle with the PM100D Console and S130C Slim
725 Photodiode Sensorlight (Thorlabs). Every pacing stimulation (including 8 Hz) was performed
726 using 5 ms square pulses. To apply scrambled light stimulation, we used an Arduino
727 microcontroller to generate a white noise oscillation signal directly fed into the analogue input
728 of the laser diode driver. To perform randomly selected frequency stimulation, we used a
729 standard 5s ON, 5s OFF protocol but for each stimulation epoch, we used an Arduino
730 microcontroller to randomly select a stimulation frequency in the theta band. When applying
731 optogenetic stimulation during behavior, a loose piece of heat shrink tubing was fitted around
732 the junction between the patch cord and the mouse' ferrule implant to limit visible light
733 emission. Light intensities are expressed as nominal power, as measured at the tip of the fiber
734 optic implant - cord assembly, and corrected for the appropriate wavelength.

735

736 **Behavioral assays**

737 *Sequential tone linear track*

738 Mice were water scheduled and could access water only for 2h per day from 6-8 pm. To
739 disentangle spatial, temporal, and distance codes, we build a 134 cm long linear track using
740 medium gray Lego® bricks which allows easy modifications and implementations without the
741 need to permanently modify the structure of the maze. Pyroelectric sensors were placed in
742 each end of the linear track, and were connected to an Arduino microcontroller. Each
743 detection triggered a new tone in sequence, indicating the progress to reward delivery. The
744 following tones were used and delivered using a piezo speaker: 1Hz beeps at 2,000Hz, 4Hz
745 beeps at 3,000Hz, and a continuous tone at 4,000Hz. When the last, continuous tone was
746 triggered, a reward (10% sucrose in water) was delivered at the starting end of the linear track
747 in the cap of a 15 mL Falcon tube. Changes in running direction before triggering the next
748 tone were considered as errors and did not trigger reward delivery. Performance was
749 measured as the number of correct runs (with no error) divided by the number of total runs.

750

751 *Novel object place recognition*

752 On the first day, mice were allowed to freely explore a 45x45 cm dark gray open-field that
753 contained visual cues (large white horizontal and vertical gratings) on its walls for 10 min. On
754 the second day, two identical objects (helping hand base) were presented for 10 min. On the
755 third day, mice were allowed to explore the same open field while the location of one of the
756 two objects was displaced. To control for potential spatial preference biases, both the initial as
757 well as the displaced position of objects were randomized. Mice were attributed a random
758 testing order that was kept identical throughout the three days of testing. Behavior was
759 recorded with a video camera and analyzed offline. Behavioral analysis was performed blind

to the genotype and treatment. Object explorations were defined as epochs where mice have their nose within 1 cm of an object. Recognition index (RI) was computed as the following:

$$RI = \frac{t_{novel}}{t_{novel} + t_{familiar}}$$

where t_{novel} and $t_{familiar}$ represent the time exploring novel and familiar objects, respectively. This metric can also be computed in the sample phase for the prospectively novel (displaced) object to assess potential pre-existing preferential biases.

Automated delayed non-match to sample task

Mice were water-scheduled and trained in a continuous T-maze to a delayed non-match to sample task. Briefly, each trial was divided into two phases: sample and test. In the sample phase, one arm was blocked and mice were forced to explore the opposite arm where they received a 50 µL of 10% sucrose water reward. After completing the sample phase, mice were subjected to a delay (10 s). Then, during the test phase, both arms could be explored, but only the opposite (unexplored) arm is baited, so that mice have to alternate locations between sample and test phases. Mice were subjected to 10 trials (sample + test) per day, for 10 consecutive days, and the daily success rate was calculated at the number of correct choices divided by the total number of trials.

Post-mortem histological analyses

780 After completion of behavioral testing, mice were deeply anesthetized with a mixture
781 ketamine/xylazine/acepromazide (100, 16, 3 mg/kg, respectively, intraperitoneal injection)
782 and perfused transcardially with 4% paraformaldehyde (PFA) in PBS. Brains were extracted
783 and postfixed overnight in PFA at 4 ºC and subsequently washed in PBS for an additional 24
784 h at 4 ºC. Brains and sections were cryoprotected in a solution of 30 % ethylene glycol, 30 %
785 glycerol, and 40 % PBS until used. Each brain was then sectioned at 50 µm using a
786 vibratome: every section was sequentially collected in 4 different 1.5 mL tubes to allow
787 different analyses (electrode location, immunohistochemistry).

788

789 *Immunohistology*

790 Using one tube of collected brain sections (25% sampling) for each analysis, sections were
791 washed 3x5 min in PBS to remove cryoprotective solution. Sections were first incubated
792 overnight with PGT (0.45 % Gelatin and 0.25 % Triton in PBS) at 4 ºC. Next, slices were
793 incubated with primary antibodies: either 1:200 goat anti-choline-acetyl-transferase from
794 Millipore or 1:500 mouse anti-parvalbumin monoclonal IgG1 from Sigma-Aldrich in PGT at
795 room temperature for 48 h or 2 h respectively. Following washes of 10, 20, and 30 min,
796 sections were then incubated with secondary antibodies [1:2000 donkey anti-goat coupled
797 with Alexa 488 or 1:500 goat anti-mouse IgG1 coupled to Alexa 488 (Life Technologies)] in
798 PGT for 45 min. Following 10, 20, and 30 min washes, sections were then mounted on glass
799 slides and permanently coverslipped with Fluoromount mounting medium that contained
800 DAPI. Only mice with histologically confirmed placement of implants were included in this
801 study. For GRIN lenses, the surface of the lens had to be < 100µm above *stratum pyramidale*
802 and GCaMPf expression was confirmed using fluorescence microscopy. Electrophysiological

803 implants had to include at least one microelectrode in CA1 *stratum radiatum* or *stratum*
804 *pyramidale*. Finally, the tips of fiber optics had to be within 100 µm of the medial septum
805 region, and proper construct expression was assessed using fluorescence microscopy.

806

807 **Data analysis**

808 *Automatized tracking of behavior*

809 To extract information about the position, velocity, and head direction of mice, we used
810 DeepLabCut[68,69]. Briefly, we trained a model to detect mice ears, nose, body, and tailbase.
811 Head direction was estimated using the angle between either each ear or the nose and body
812 depending on measurement availability. Location data was interpolated to calcium imaging
813 sampling frequency using linear interpolation. Velocity was extracted by computing $\Delta d/\Delta t$
814 where d is the distance and t time, and subsequently smoothed the result by applying a
815 gaussian filter with sigma = 33 ms to remove movement artifacts. Velocity signals were used
816 to identify periods of locomotor activity, using a threshold of 5 $cm.s^{-1}$, and used selectively to
817 compute place, time, and distance modulation of activity.

818

819 *Calcium imaging analysis*

820 Calcium imaging data analysis was performed using MATLAB 2020a and Python 3.8.4.
821 Video recordings were analyzed using the Miniscope Analysis pipeline
822 (https://github.com/etterguillaume/MiniscopeAnalysis). Briefly, rigid (rotation and
823 translation) motion correction was applied using NoRMCorre[70], and videos were spatially
824 downsampled (3x) before concatenation. Calcium traces were extracted using CNMFe[51] using

the following parameters: gSig = 3 pixels (width of gaussian kernel), gSiz = 20 pixels (approximate neuron diameter), background_model = 'ring', spatial_algorithm = 'hals', min_corr = 0.8 (minimum pixel correlation threshold), min_PNR = 8 (minimum peak-to-noise ratio threshold).

Raw calcium traces were filtered to remove high-frequency fluctuations and binarized: briefly, neurons were considered active when normalized calcium signal amplitude > 2 standard-deviations, and first-order derivative > 0 (see Etter et al., 2020 for additional details on the methodology[52]). To extract neurons tuning to specific variables, location, time, and distance were binned (location: 3 cm bins; time: 1 s bins; distance: 3 cm bins). From binarized signals, we computed the marginal likelihood of cells being active $P(A)$ that we use as a proxy for neuronal activity. More importantly, we then derive activity likelihood, or the 'probability of being active given the state of a variable' $P(A|S_i)$using binned variables:

$$P(A|S_i) = \frac{time\ active\ within\ bin\ i}{time\ within\ state}$$

where A is the activity level (0 or 1) of a given neuron, when being in bin i of a given state S.

To identify place, time, and distance cells, we computed the mutual information (MI) between neuronal activity and the bin i of a given state S using the following:

$$MI = \sum_{i=1}^{M} \sum_{j=1}^{2} P(S_i \cap A_j) \times \log 2 \frac{P(S_i \cap A_j)}{P(S_i) \times P(A_j)})$$

where M is the total number of possible behavioral states, $P(S_i \cap A_j)$ is the joint probability of the animal being in bin i concurrently with activity level j (0 or 1). To assess the significance of the obtained MI value, we then generated n = 1000 shuffled surrogates using random circular permutations. We chose circular permutations because they remove the temporal

847 relationship between neuronal activity and behavior, while still preserving the temporal
848 structure of calcium transients and therefore leads to more conservative results (as opposed to
849 complete randomization of every data point, which inflates the significance value of results).
850 Because shuffled surrogates were not systematically normally distributed, we used a non-
851 parametric approach where the *p*-value (p_N) corresponds to the number of datapoints from the
852 shuffled distribution that are greater than the actual data for each bin, divided by the number
853 of permutations[52,71].

854 To determine the modulation of cells by optogenetic stimulations, we used a similar
855 approach but computed the MI between neuronal activity and the binarized stimulation
856 signals (thus treated as a behavioral state). The same circular shuffling procedure was then
857 used to extract statistical significance.

858

859 *Naive Bayes decoder*

860 To further evaluate the significance of neuronal activity at the population level, we
861 trained a naive Bayesian decoder with a uniform prior to predict spatiotemporal variables
862 from binarized neuronal activity. The posterior probability density function, which is the
863 probability that an animal is in a particular bin S_i, given the neural activity A is calculated
864 using the following equation:

865 $$P(S_i|A)=\frac{P(A|S_i)\times P(S_i)}{P(A)}$$

866 where P(S|A) is the posterior probability distribution of states given neuronal activity. Using
867 only epochs with velocity > 5 cm/s, a training dataset was generated using 50% of the data.
868 The remaining 50% of the data was used for testing. Decoding error was calculated using 50

bootstrapped surrogates and a pool of 100 cells using randomly chosen data points with replacement. Every neuron is assumed to be independent of each other, which in practice is not the case and leads to greater reconstruction errors, but decreases computational time. The population posterior probability was derived from the following equation:

$$P(S|A)=\prod_{k=1}^{N}\frac{P(A_k|S)\times P(S)}{P(A_k)}$$

with N corresponding to the number of neurons used. Finally, the decoded data point corresponds to the maximum *a posteriori* (MAP):

$$\hat{y}=arg\,max\exp\left[\sum_{k=1}^{N}\log\left(1+\frac{P(A_k|S)\times P(S)}{P(A_k)}\right)-1\right]$$

The exponential-logarithm trick is used to prevent underflow when multiplying a large number of small probabilities, which is a correct approximation since the posterior is a smooth convex function.

While many studies utilize temporal smoothing, we did not use any here since we want to observe the unaltered temporal codes of time-modulated cells, and temporal smoothing can lead to displacement of tuning curves[52]. On the linear track, decoding error was assessed as:

$$decoding\,error=|decoded\,state-actual\,state|$$

In order to compare decoding scores across animals, we z-scored decoding errors using the following equation:

$$z=\frac{\bar{x}-\bar{s}}{\sigma(x)}$$

where $\bar{x}$ is the average actual decoding error, $\bar{s}$ is the average decoding error using shuffled surrogates, and $\sigma(x)$ is the standard deviation of the actual decoding error.

Tracking cells over multiple days

Neurons were tracked over multiple days using a probabilistic method as previously described[72]. Briefly, spatial footprints were aligned using rigid alignment to correct for rotations and translations. After alignment, we considered candidate sets of cells to be the same neuron if their maximal distance was < 12 um, and used the modeled spatial correlation threshold (usually in the range .6 - .8) to determine the identity of cell pairs across days. Finally, we assessed the stability of the spatial representation using pairwise field correlation (Pearson correlation of tuning curves).

Electrophysiological analysis

Electrophysiological data analysis was performed using MATLAB 2020a and both the signal processing as well as the wavelet toolbox. Wavelet convolution was applied to LFP signals using complex Morlet wavelets ('cmor1-1.5' in MATLAB) when both time- and frequency-domain accuracy was required. Moving window Fourier convolution (2 s window in the theta band, 5 s window in the gamma band, 10 ms moving steps) was used when frequency-domain accuracy was privileged over time-domain accuracy (e.g. to plot dominant frequency when pacing using optogenetics). To monitor sharp-wave ripples (SWRs), mice were allowed to freely explore an open-field for 10 min while recording. Stimulations (scrambled or 8 Hz) were performed with a 5s ON, 5s paradigm. Only periods of quiet restfulness were considered

914 for analysis. To this end, we computed the z-scored ratio of theta/delta power after filtering
915 for each frequency band and performing a Hilbert transform, as described previously[73], and
916 only considered periods where the resulting value was under 0. To detect SWRs, we filtered
917 LFP signals in the 150-250 Hz frequency band and subsequently z-scored. Ripples were
918 detected using the findpeaks function in MATLAB, with the following parameters:
919 threshold=4 sd, minpeakwidth=0 s, minpeakdistance=0.03 s.

920

921 **Statistics**

922 Unless stated otherwise, all data are presented as mean ± standard error of the mean (SEM)
923 and statistical test details are described in the corresponding results. The distribution
924 normality of each group was assessed using Shapiro-Wilk normality test and parametric tests
925 were used only when distributions were found normal (non-parametric tests are described
926 where applicable). 1ANOVA: one-way ANOVA; 2ANOVA: two-way ANOVA; RM-
927 ANOVA: repeated measure ANOVA. $p < 0.05$ was considered statistically significant. *, $p <$
928 0.05; **, $p < 0.01$; ***, $p < 0.001$, ****, $p < 0.0001$.

929

930

931 **Author information**

932 **Affiliations**

933 McGill University & Douglas Mental Health University Institute, Montreal, Canada

934 Corresponding authors: sylvain.williams@mcgill.ca, etterguillaume@gmail.com

935 6875 Boulevard LaSalle, Verdun, QC H4H 1R3, Phone : 514 761-6131, Fax: 514 888-4067

936

937 **Contributions**

938 GE and SW designed the study. GE performed and analyzed *in vivo* experiments. SVDV
939 performed and analyzed both behavioral as well as immunohistological experiments. JC
940 performed surgeries for the mice used for controlling cross-talk between calcium imaging and
941 optogenetics. GE and SW wrote the manuscript with inputs from all collaborators.

942

943 **Competing interests**

944 The authors declare no competing interests.

945

946 **Correspondence author**

947 Correspondence should be addressed to Sylvain Williams: sylvain.williams@mcgill.ca

948

949 **Acknowledgements**: We thank Ke Cui for helping to maintain the colony and perfusing
950 mice; Mark P Brandon, Alexandra Keinath, and Eric Carmichael for comments on the
951 manuscript.

952

Funding

This work was supported by funding from the Canadian Institutes for Health Research (CIHR) Foundation Program FDN-148478, the Natural Sciences and Engineering Research Council of Canada (NSERC) Discovery Grant RGPIN-2020-06717, and a Tier 1 Canada Research Chair to SW. SVDV was supported by a Vanier Canada Graduate Scholarship and the Richard H. Tomlinson Doctoral Fellowship. JC was supported by a Healthy Brains, Healthy Lives (HBHL) Graduate Student Fellowship and a McGill Integrated Program in Neuroscience (IPN) Internal Student Award. The funders had no role in study design, data collection and analysis, decision to publish, or preparation of the manuscript.

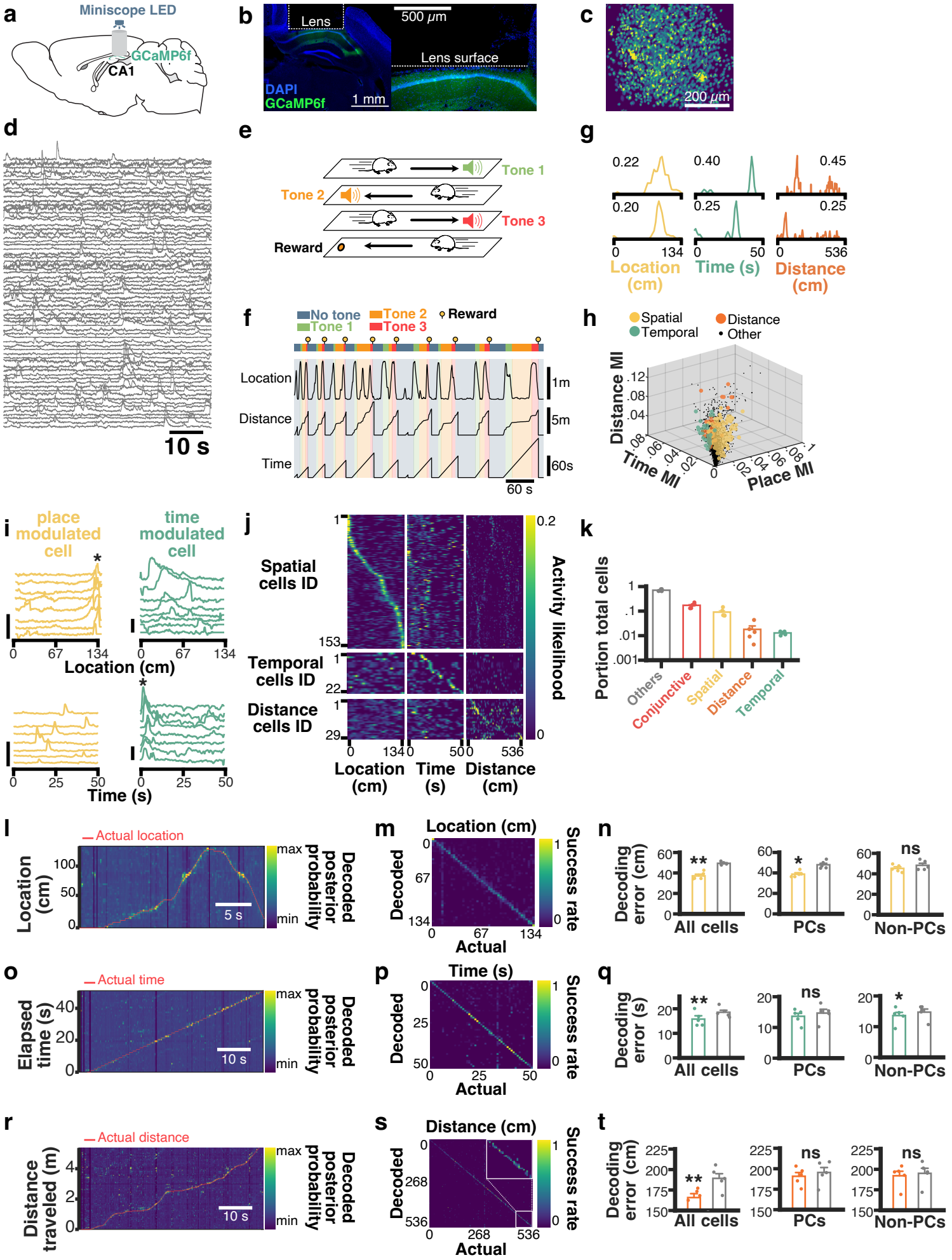
a
Miniscope LED
GCaMP6f
CA1
b
Lens
500 μm
Lens surface
DAPI
GCaMP6f
1 mm
c
200 μm
d
10 s
e
Tone 1
Tone 2
Tone 3
Reward
g
0.22
0.40
0.45
0.20
0.25
0.25
0
134
0
50
0
536
Location (cm)
Time (s)
Distance (cm)
f
No tone
Tone 2
Reward
Tone 1
Tone 3
Location
Distance
Time
1m
5m
60s
60 s
h
Spatial
Distance
Temporal
Other
Distance MI
Time MI
Place MI
i
place modulated cell
time modulated cell
Location (cm)
Time (s)
j
Spatial cells ID
Temporal cells ID
Distance cells ID
Activity likelihood
Location (cm)
Time (s)
Distance (cm)
k
Portion total cells
Others
Conjunctive
Spatial
Distance
Temporal
l
Actual location
Location (cm)
5 s
max
min
Decoded posterior probability
m
Location (cm)
Decoded
Actual
Success rate
n
Decoding error (cm)
All cells
PCs
Non-PCs
ns
o
Actual time
Elapsed time (s)
10 s
p
Time (s)
q
Decoding error (s)
r
Actual distance
Distance traveled (m)
s
Distance (cm)
t

FIGURE 1

Figure 1. Spatial and temporal codes are present in partially overlapping populations of CA1 neurons. a, mice were injected with GCaMP6f in hippocampal subfield CA1 and subsequently implanted with a GRIN lens over the pyramidal cell layer for miniscope imaging. **b**, post-mortem coronal section from one example mouse. blue, DAPI; green, GCaMP6f. **c**, planar projection of extracted spatial footprints from one example mouse. **d**, corresponding calcium transients from a portion of recorded cells. **e**, behavioral paradigm used to disentangle time, place, and distance coding cells (see Methods). **f**, behavioral signals from one example mouse. **g**, example pairs of neurons modulated by place (yellow), time (green), or distance (orange) along with corresponding peak activity likelihood. **h**, 3D scatter plot of the distribution of cells selectively encoding a single variable along with their associated mutual information (MI) in each dimension. Cells in black either encode more than one variable or did not encode any variable significantly more than shuffled surrogates. **i**, individual traces from one example place-modulated cell (yellow) and one example time-modulated cell (green). Vertical scale bars: 1ΔF/F. **j**, tuning curves for place, time, and distance cells, sorted by the location of peak activity likelihood for each dimension (location, time, and distance). **k**, portion of total cells (log scale) encoding for one, several, or no variables. Bayesian decoding of location (**l-n**), time (**o-q**), and distance (**r-t**). For each encoded variable, posterior probabilities are plotted with the corresponding actual state (**l,o,r**). Confusion matrices between the actual vs decoded values (**m,p,s**). Decoding errors using all cells, place cells only, or all but place cells (**n,q,t**).

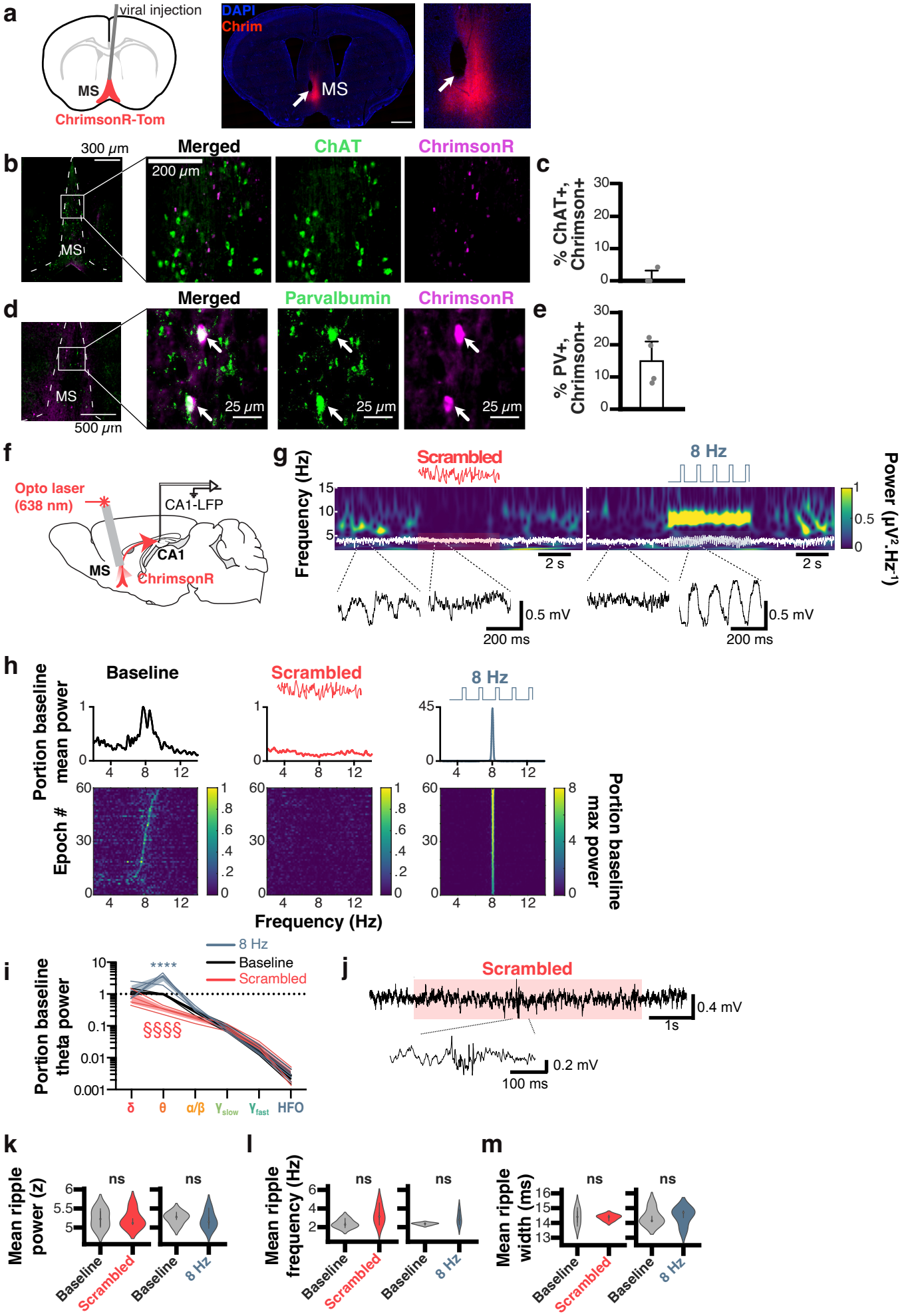
a
viral injection
MS
ChrimsonR-Tom
DAPI
Chrim
MS
b
300 μm
Merged
ChAT
ChrimsonR
200 μm
MS
c
% ChAT+, Chrimson+
d
Merged
Parvalbumin
ChrimsonR
MS
500 μm
25 μm
e
% PV+, Chrimson+
f
Opto laser (638 nm)
CA1-LFP
CA1
MS
ChrimsonR
g
Scrambled
8 Hz
Frequency (Hz)
Power (μV².Hz⁻¹)
2 s
0.5 mV
200 ms
h
Baseline
Scrambled
8 Hz
Portion baseline mean power
Epoch #
Portion baseline max power
Frequency (Hz)
i
8 Hz
Baseline
Scrambled
Portion baseline theta power
****
§§§§
δ
θ
α/β
γslow
γfast
HFO
j
Scrambled
0.4 mV
1s
0.2 mV
100 ms
k
Mean ripple power (z)
ns
Baseline
Scrambled
8 Hz
l
Mean ripple frequency (Hz)
m
Mean ripple width (ms)

FIGURE 2

Figure 2. Selective optogenetic pacing and ablation of theta oscillations. a, AAV-ChrimsonR expressing vector was injected in the MS (blue, DAPI; red, ChrimsonR) and a fiber optic was placed at the injection site (white arrow). Scale bar, 1mm. **b**, immunohistological double staining for ChrimsonR and parvalbumin (PV+) neurons. **c**, quantification of ChrimsonR+/PV+ co-expressing neurons. **d**, immunohistological double staining for ChrimsonR and cholinergic (ChAT+) neurons. **e**, quantification of ChrimsonR+/ChAT+ co-expressing neurons. **f**, recording configuration, with fiber optic in the MS and electrode in CA1. **g**, wavelet spectrograms before, during, and after scrambled (left, in red) and 8 Hz (right, in blue) stimulation patterns, with associated unfiltered LFP (white overlay, and enlarged, black traces at the bottom). **h**, average Fourier power spectra for 60 x 5s stimulation epochs (top), and sorted power spectra for each stimulation epoch (bottom) for baseline (left, in black), scrambled (center, in red), and 8 Hz (right, in blue) stimulations in a representative mouse. **i**, group average (n = 4 mice) portion of baseline power for each stimulation pattern and every frequency band (log scale). Frequency bands: δ, 1-4 Hz; θ, 4-12 Hz; α/β, 12-30 Hz; γ_{slow}, 30-60 Hz; γ_{fast}, 60-120 Hz; HFO (high frequency oscillations), 120-250 Hz. **j**, example unfiltered trace of a ripple event during a scrambled optogenetic stimulation epoch. **k**, mean z-scored ripple power during baseline and either 8 Hz (blue) or scrambled (red) stimulations. **l**, same for mean ripple frequency of occurrence. **m**, mean ripple width.

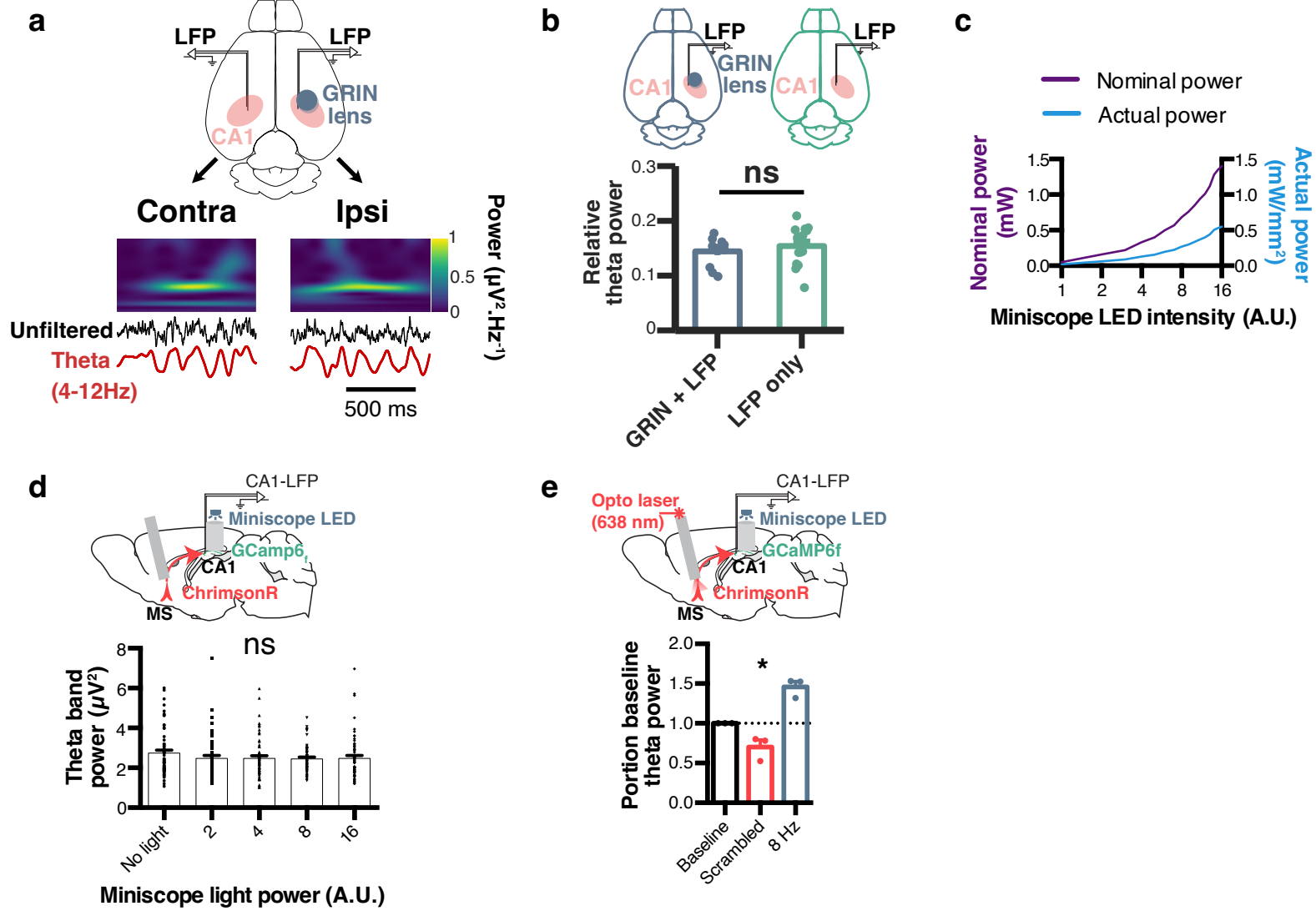
a
LFP
LFP
GRIN lens
CA1
Contra
Ipsi
Power (μV².Hz⁻¹)
1
0.5
0
Unfiltered
Theta (4-12Hz)
500 ms
b
LFP
LFP
GRIN lens
CA1
CA1
ns
Relative theta power
0.3
0.2
0.1
0
GRIN + LFP
LFP only
c
Nominal power
Actual power
Nominal power (mW)
Actual power (mW/mm²)
1.5
1.0
0.5
0.0
1
2
4
8
16
Miniscope LED intensity (A.U.)
d
CA1-LFP
Miniscope LED
GCamp6f
CA1
ChrimsonR
MS
ns
Theta band power (μV²)
8
6
4
2
0
No light
2
4
8
16
Miniscope light power (A.U.)
e
CA1-LFP
Opto laser (638 nm)
Miniscope LED
GCaMP6f
CA1
ChrimsonR
MS
*
Portion baseline theta power
2.0
1.5
1.0
0.5
0.0
Baseline
Scrambled
8 Hz

FIGURE 3

Figure 3. GRIN lens implant does not affect theta oscillations and enables combined calcium imaging and optogenetics. a, diagram showing recording configuration (horizontal plane), with LFP electrodes in CA1 of both hemispheres, and a GRIN lens only in the right hemisphere (top). Example theta oscillations recorded in both hemispheres using wavelet spectrograms, raw (black) and theta filtered (red) traces. **b**, relative theta power measured in the right hemisphere of mice implanted with electrodes and GRIN lenses (blue) versus electrodes only (green). **c**, the relationship between miniscope LED input value and measured nominal power (purple) as well as actual light power corrected for the surface of a GRIN lens (blue). **d**, corresponding theta power from LFP electrode attached to GRIN lens when using different miniscope LED emitting light power values (in the absence of optogenetic stimulations). **e**, effects of MS optogenetic stimulations on theta oscillations during miniscope blue light emission through the lens (8AU LED power, corresponding to ~0.3mW/mm^2).

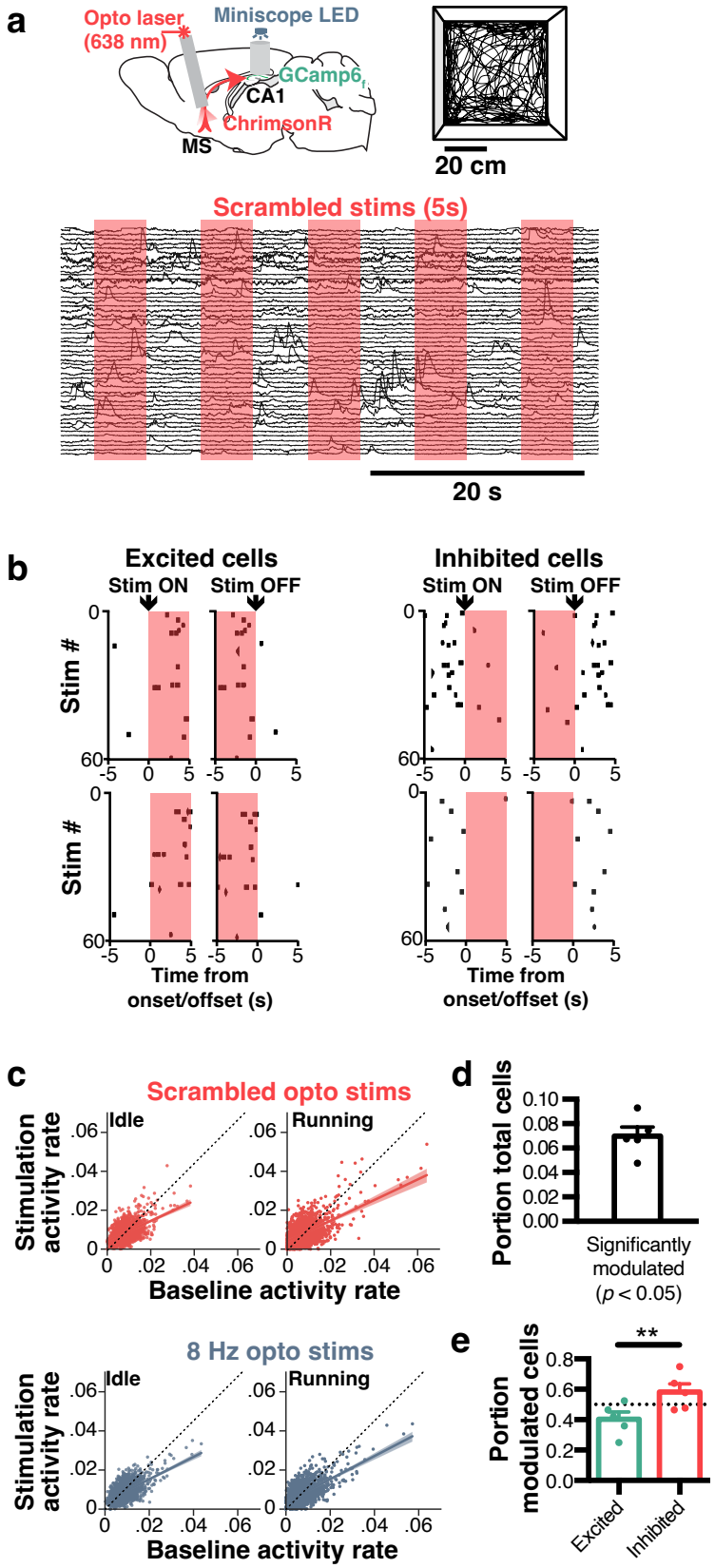
a
Opto laser (638 nm)
Miniscope LED
GCamp6f
CA1
ChrimsonR
MS
20 cm
Scrambled stims (5s)
20 s
b
Excited cells
Inhibited cells
Stim ON
Stim OFF
Stim #
Time from onset/offset (s)
c
Scrambled opto stims
Idle
Running
Stimulation activity rate
Baseline activity rate
8 Hz opto stims
d
Portion total cells
Significantly modulated ($p < 0.05$)
e
Portion modulated cells
**
Excited
Inhibited

FIGURE 4

Figure 4. MS optogenetic stimulation modulates the activity of a subpopulation of CA1 pyramidal cells. a, recording CA1 neurons during MS optogenetic stimulation (5s ON, 5s OFF) while simultaneously imaging CA1 neurons in mice freely exploring an open field. **b**, peristimulus time raster plot of binarized activity for pairs of excited (left) or inhibited (right) neurons. **c**, scatter plot for all pooled neurons (n = 1849 cells, N = 5 mice) of activity probability during baseline vs stimulation (red, top: scrambled; blue, bottom: 8 Hz), for both idle (left) and running (right) periods. **d**, portion of total cells significantly modulated by stimulations (N = 5 mice). **e**, portion of modulated cells that are excited (green) or inhibited (red).

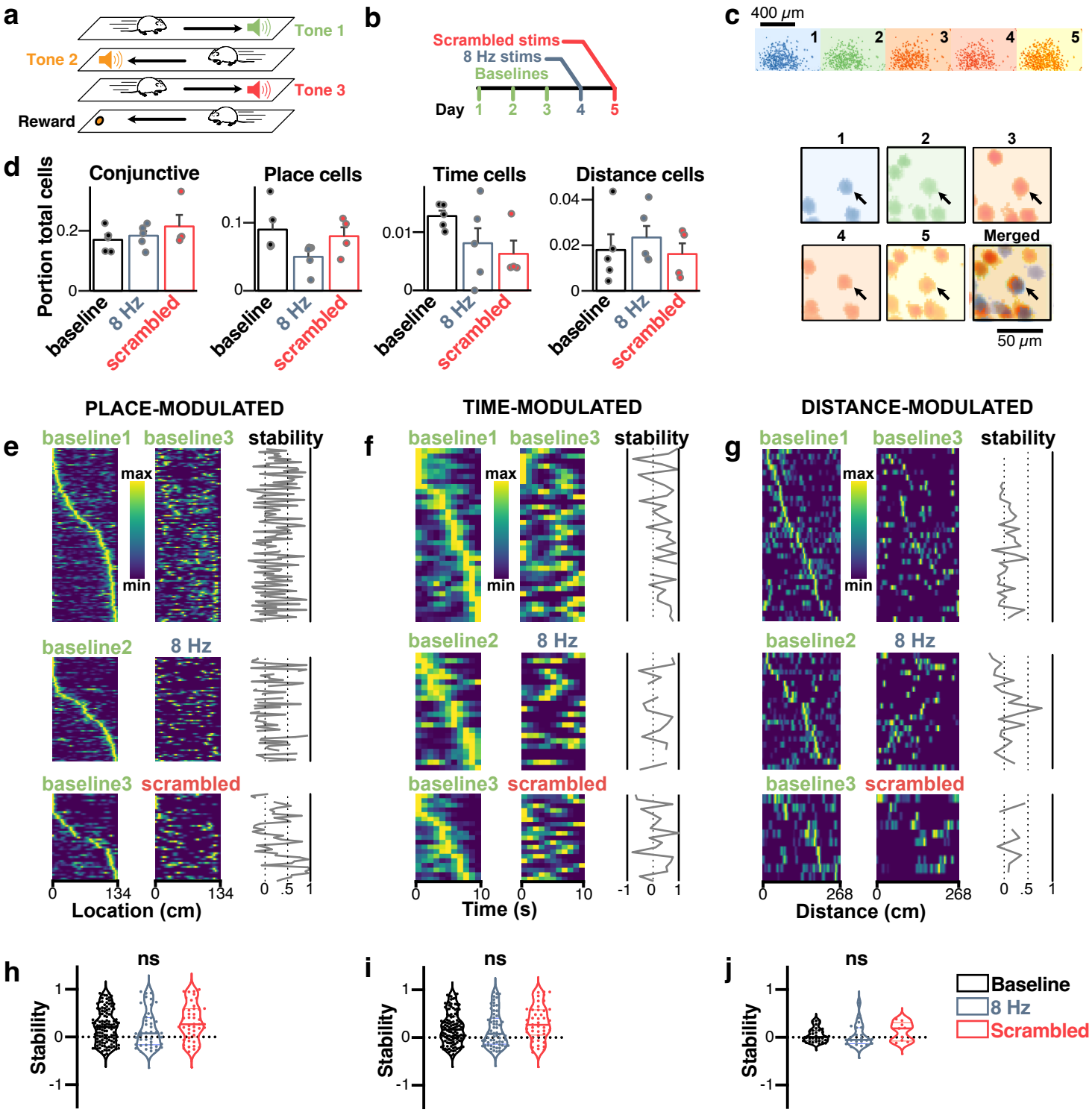
a
Tone 1
Tone 2
Tone 3
Reward
b
Scrambled stims
8 Hz stims
Baselines
Day 1 2 3 4 5
c
400 μm
1 2 3 4 5
1 2 3
4 5 Merged
50 μm
d
Portion total cells
Conjunctive
Place cells
Time cells
Distance cells
baseline
8 Hz
scrambled
PLACE-MODULATED
TIME-MODULATED
DISTANCE-MODULATED
e
f
g
baseline1
baseline3
stability
max
min
baseline2
8 Hz
baseline3
scrambled
Location (cm)
Time (s)
Distance (cm)
h
i
j
ns
Stability
Baseline
8 Hz
Scrambled

FIGURE 5

Figure 5. MS optogenetic stimulation does not disrupt the stability of spatiotemporal codes. **a**, we recorded mice on the 3-tone linear track to identify time-, place- and distance-modulated cells (see fig. 1 and Methods). **b**, experimental timeline. **c**, spatial footprints of neurons recorded over days and comparison scheme used to assess stability (top). Example neuron (black arrow) tracked over the 5 experimental days (bottom). **d**, portion of total cells encoding for one or several (conjunctive) variables before and during 8 Hz and frequency scrambling optogenetic stimulations (N = 5 mice). **e**, sorted place fields for identified place cells across day pairs. The first day is used as a baseline and mice undergo 8 Hz, scrambled, or no stimulations (control treatment) during the other day. Stability is computed as the pairwise correlation of fields between the two-day pairs. **f**, same for time-modulated cells. **g**, same for distance-modulated cells. **h**, corresponding average stability for place-modulated cells (each dot represents a cell pooled from N = 5 mice). **i**, same for time-modulated cells. **j**, same for distance modulated cells.

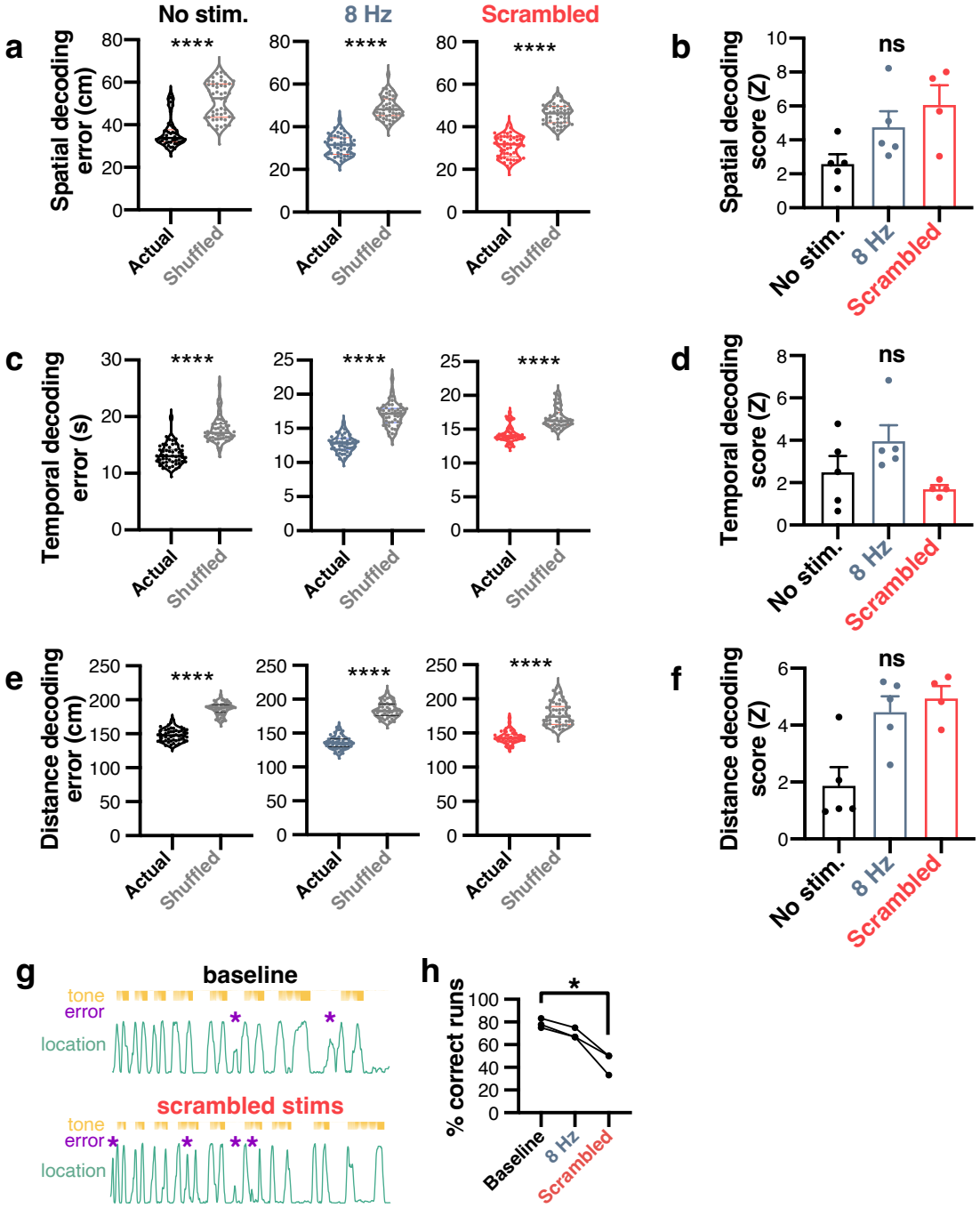
a
No stim.
8 Hz
Scrambled
Spatial decoding error (cm)
****
Actual
Shuffled
b
Spatial decoding score (Z)
ns
No stim.
8 Hz
Scrambled
c
Temporal decoding error (s)
d
Temporal decoding score (Z)
e
Distance decoding error (cm)
f
Distance decoding score (Z)
g
baseline
tone
error
location
scrambled stims
h
% correct runs
*
Baseline
8 Hz
Scrambled

FIGURE 6

Figure 6. MS optogenetic stimulation alters behavior but does not disrupt spatiotemporal codes. Using a naive Bayesian classifier, location (**a**,**b**), time elapsed (**c**,**d**), and distance traveled (**e**,**f**) were predicted from CA1 neuronal activity. **a**,**c**,**e**, decoding error (euclidean distance) for baseline, 8 Hz, and scrambled optogenetic stimulation conditions for location, time, and distance, respectively (computed in a representative mouse). **b**,**d**,**f**, decoding z-score (higher values indicate better decoding compared to shuffled surrogate) for location, time, and distance, respectively, using N = 5 mice. **g**, example scoring of errors (purple stars) in the tone-cued linear track task. **h**, percent of correct runs during baseline, 8 Hz, and scrambled stimulations.

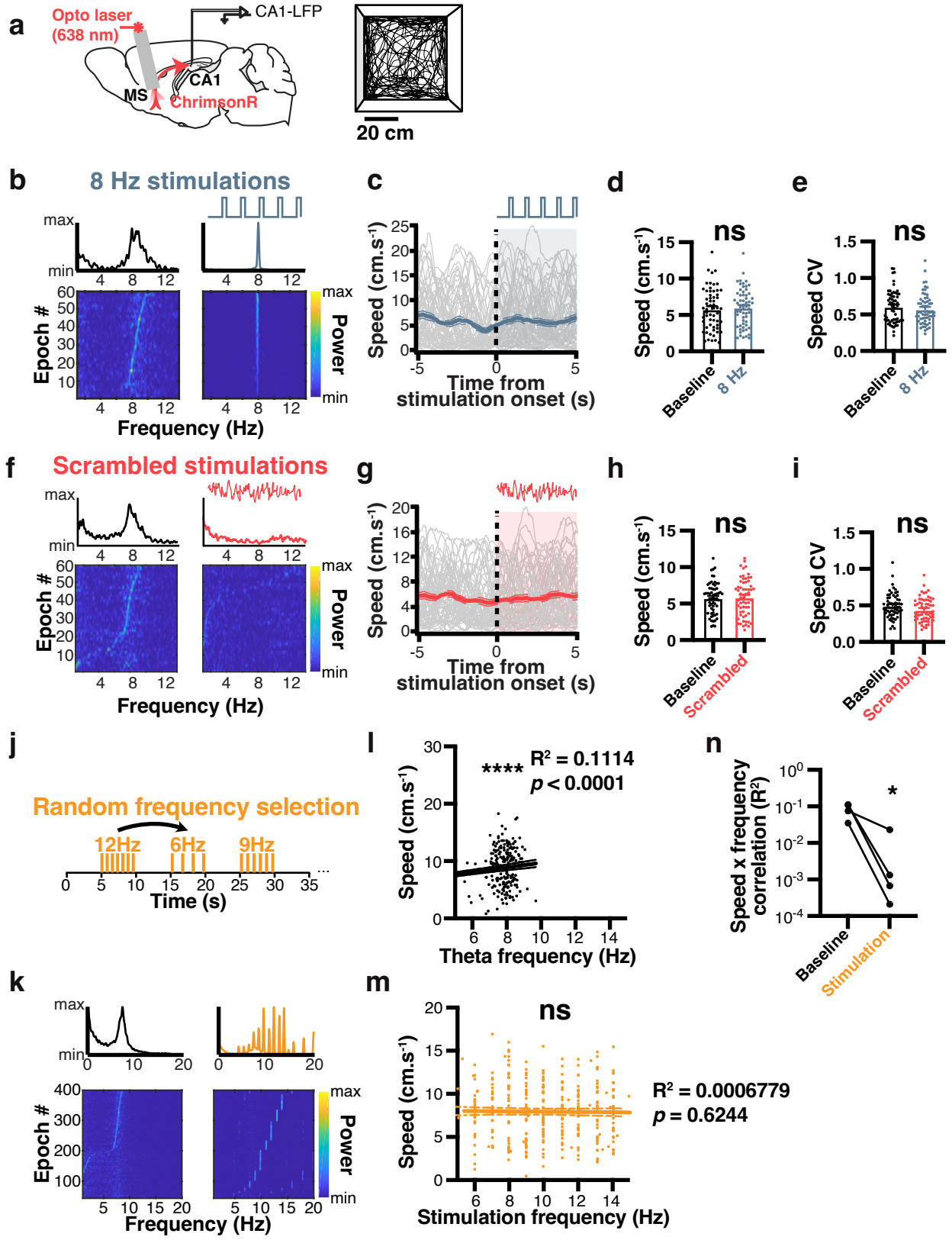
a
Opto laser
(638 nm)
CA1-LFP
CA1
MS
ChrimsonR
20 cm
b
8 Hz stimulations
max
min
Epoch #
Frequency (Hz)
Power
c
Speed (cm.s-1)
Time from
stimulation onset (s)
d
ns
Speed (cm.s-1)
Baseline
8 Hz
e
ns
Speed CV
Baseline
8 Hz
f
Scrambled stimulations
g
h
ns
Baseline
Scrambled
i
ns
j
Random frequency selection
12Hz
6Hz
9Hz
Time (s)
l
****
R² = 0.1114
p < 0.0001
Theta frequency (Hz)
n
Speed x frequency correlation (R²)
*
Baseline
Stimulation
k
m
ns
R² = 0.0006779
p = 0.6244
Stimulation frequency (Hz)

FIGURE 7

Figure 7. MS optogenetic stimulation does not control locomotor speed. a, mice were implanted with fiber optics in the MS after transfecting ChrimsonR, implanted with an electrode in CA1 (left), and freely explored an open field (right). **b**, average Fourier power spectra for 60 x 5s stimulation epochs (top), and sorted power spectra for each stimulation epoch (bottom) for baseline (left, in black), and 8 Hz (right, in blue) stimulations in one example mouse. **c**, peristimulus time plot of locomotor speed before and during 8 Hz MS optogenetic stimulation. Average speed in blue (line thickness indicated SEM). **d**, average locomotor speed before and during 8 Hz MS optogenetic stimulation. **e**, locomotor speed coefficient of variation (CV) before and during stimulation. **f**, average Fourier power spectra for 60 x 5s stimulation epochs (top), and sorted power spectra for each stimulation epoch (bottom) for baseline (left, in black), and scrambled (right, in red) stimulations in one example mouse. **g**, peristimulus time plot of locomotor speed before and during scrambled MS optogenetic stimulation. Average speed in red (line thickness indicated SEM). **h**, average locomotor speed before and during scrambled MS optogenetic stimulation. **i**, locomotor speed coefficient of variation (CV) before and during stimulation. **j**, random frequency generator used to pace theta oscillations at varying frequencies (see Methods). **k**, average Fourier power spectra for 400 x 5s stimulation epochs (top), and sorted power spectra for each stimulation epoch (bottom) for baseline (left, in black), and randomly selected (right, in orange) stimulations in one example mouse. **l**, relationship between locomotor speed and natural (unstimulated) theta frequency. **m**, same but during pacing of theta oscillations at varying stimulation frequencies. **n**, correlation between speed and natural (black) or controlled (orange) theta oscillations in N = 4 mice.

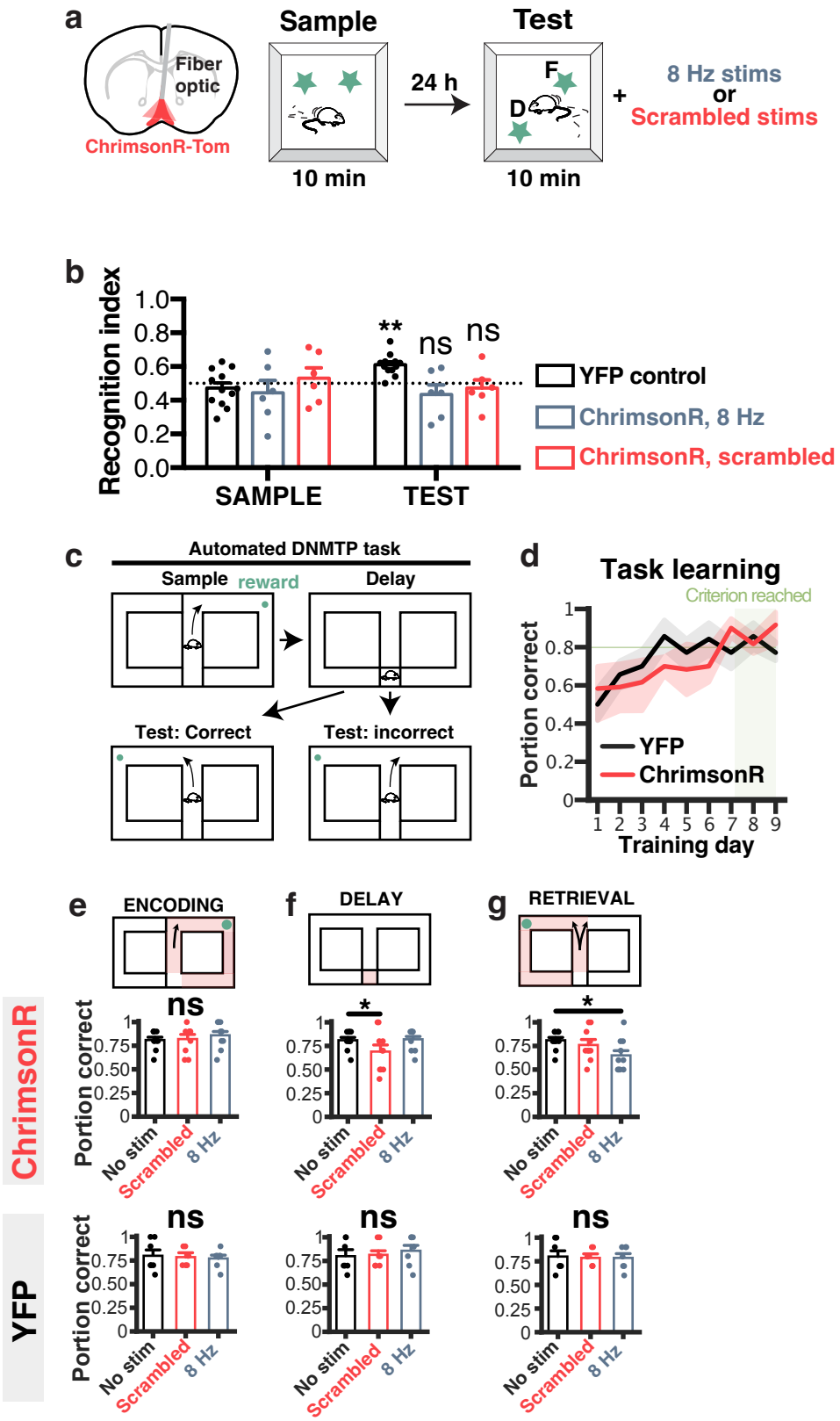
a
Fiber optic
ChrimsonR-Tom
Sample
10 min
24 h
Test
F
D
10 min
+
8 Hz stims
or
Scrambled stims
b
Recognition index
1.0
0.8
0.6
0.4
0.2
0.0
**
ns
ns
SAMPLE
TEST
YFP control
ChrimsonR, 8 Hz
ChrimsonR, scrambled
c
Automated DNMTP task
Sample
reward
Delay
Test: Correct
Test: incorrect
d
Task learning
Criterion reached
Portion correct
YFP
ChrimsonR
Training day
e
ENCODING
f
DELAY
g
RETRIEVAL
ChrimsonR
YFP
Portion correct
ns
*
No stim
Scrambled
8 Hz

FIGURE 8

Figure 8. MS optogenetic stimulations disrupt maintenance and retrieval, but not encoding of episodic and working memory. a, mice were implanted with fiber optics in the MS after transfecting ChrimsonR (top). They were then subjected to the novel object place recognition task (bottom, see Methods). **b**, in this task, both scrambled (red) and 8 Hz (blue) disrupted memory performance when stimulating during the test phase. **c**, to further examine the effect of MS stimulation on memory encoding, maintenance, and retrieval, mice were trained in a delayed non-match to sample (DNMTS) task in an automated T-maze. **d**, mice were trained (in absence of stimulation) to choose the correct, non-matching arm until the performance exceeded a criterion of 0.8 portion of correct choices per day, for at least two consecutive days. **e**,**f**,**g**, performance during stimulation at different phases of the task for mice injected with ChrimonR (top) or YFP controls (bottom). Red shading indicates the stimulated regions of the maze. **e**, average daily performance when performing MS stimulations during encoding only (forced choice). **f**, average daily performance when performing MS stimulations during the 10 s delay period only. **g**, average daily performance when performing MS stimulations during the retrieval only (free choice).